LASER LITHOGRAPHY OF THIN POLYMER FILMS

LASER LITHOGRAPHY OF THIN POLYMER FILMS

By

JOHN MONTE HUDSON

B.Eng. & Soc. (McMaster) 2002

A Thesis
Submitted to the School of Graduate Studies
in Partial Fulfillment of the Requirements
for the Degree

Master of Applied Science

McMaster University

MASTER OF APPLIED SCIENCE (2004)
(Engineering Physics)

McMaster University
Hamilton, Ontario

TITLE: Laser Lithography of Thin Polymer Films

AUTHOR: John Monte Hudson, B.Eng. & Soc. (McMaster University)

SUPERVISORS: Dr. John S. Preston

Dr. Kari Dalnoki-Veress

NUMBER OF PAGES: x, 86

Abstract

Laser lithography has been implemented in many ways to pattern polymeric materials. By using a tightly focused laser beam we can induce sharp thermal gradients, exceeding 1,500,000 ^{o}C/cm, onto the surface of a thin polymer film. The temperature dependence of the surface tension in such a thermal field gives rise to a flow of material away from the center of the beam focus driven by the Marangoni or thermocapillary effect.

The evolution of a film irradiated by a focused laser can be, in a general sense, predicted by a presented hydrodynamic model, which is based on simple fluid mechanics. However, the details of the individual evolution profiles show a more complicated behaviour. It has been shown that this complex behaviour can be explained by considering the optical interference effects of the thin polymer coating. An optical feedback control routine has been developed to compensate for the interference effect by monitoring and maintaining a constant absorbed laser power. This ensures that the temperature gradient that drives the lithography process is consistent during operation.

Additional studies involving high laser power effects, different material systems and other thin film phenomena have revealed an interesting assortment of novel behaviours. The extension of these behaviours to the lithography process lead towards the development of applications in microfabriation and microfluidic devices.

Preface

In classic Hudson style I sit here, dawn approaching, putting the final touches on what will be one of the greatest achievements of my life (so far…). Dopey eyed and weary, I stare the wall and try to think of the best possible words to describe my sincere gratitude to all those that have been with me along the way. Whether it was through kindness and friendship, guidance or a stern reprimanding (for my own good), I have grown over the past two years in every dimension of my person.

Thank you John. Your easy going and humorous attitude made me at ease from the start. It was you that made my decision to pursue graduate work at McMaster a simple one. Kari. Who would have guessed that I would end up in your laboratory and would learn so much about a subject so…soft. Thank you for your patience and your trust with your expensive equipment.

Nam, Rob, Duft, Mike, Joanna, Adam, Andrew, Andrea, M.J., Michelle, Mom, Dad, Mehdi and Sarah, without your support and friendship, it just wouldn't have been worth it.

Now if you'll excuse me, I have to catch a sunrise.

J.M. HUDSON

Table of Contents

List of Figures viii

List of Tables x

1 Introduction 1
- 1.1 Laser/Matter Interactions ... 2
- 1.2 Physics and Material Properties of Polymers ... 2
  - 1.2.1 Viscosity ... 3
    - 1.2.1.1 Temperature Dependence: The WLF Equation ... 4
  - 1.2.2 Polymer Glass Transition ... 5
  - 1.2.3 Surface Tension ... 7
  - 1.2.4 The Marangoni/Thermocapillary Effect ... 8
- 1.3 Thesis Overview ... 11

2 Experimental Apparatus 12
- 2.1 General Overview of the Laser Lithography System ... 12
  - 2.1.1 Laser System ... 14
  - 2.1.2 External Shutter ... 15
  - 2.1.3 Optics Assembly ... 15
  - 2.1.4 Objective ... 15
  - 2.1.5 Sample Mount ... 17
  - 2.1.6 Translation Stages ... 17
  - 2.1.7 Power Meter ... 17
  - 2.1.8 Computer Control ... 17
- 2.2 Calibration and Operating Procedures ... 18
  - 2.2.1 Alignment Procedures ... 18
  - 2.2.2 Focusing Procedure ... 19
  - 2.2.3 Sample Levelling ... 19
  - 2.2.4 Power Meter Characterizing Procedure ... 20
  - 2.2.5 Feedback Mode (FM) ... 22
- 2.3 Sample Preparation ... 23
  - 2.3.1 Solution Preparation ... 23
  - 2.3.2 Substrate Preparation ... 24
  - 2.3.3 Spin Coating ... 24
  - 2.3.4 Post Annealing ... 24

3 **Modelling of Processes** **25**
3.1 Description of the Problem 25
3.2 The Heat Equation 27
3.2.1 The Source Term 28
3.2.1a Absorbed Intensity 28
3.2.1b Spatial Profile 29
3.2.1c Depth Profile 29
3.2.1d Time Dependency 29
3.2.1e The Complete Source Term 30
3.2.2 Boundary Conditions 30
3.3 Calculation of the Induced Surface Temperature: 31
Temperature Independent Parameters
3.3.1 The Maximum Temperature Rise 31
3.3.2 Spatial Temperature Profile 31
3.3.3 Finite Absorption 32
3.4 Calculation of the Induced Surface Temperature:
Temperature Dependent Parameters 33
3.4.1 Thermal Conductivity 33
3.4.2 Reflectivity 33
3.4.3 Absorption Coefficient 34
3.4.4 The Final Picture 34
3.5 Thin Film Interference Effects on the Temperature Rise 36
3.5.1 Reflectivity and the Fresnel Equations 36
3.5.2 Reflectance of a Thin Film 37
3.6 Temperature Calibration: Experimental Verification 40
3.6.2 Results 41

4 **Observed Patterns and Behaviours** **42**
4.1 The Working Mechanisms of Laser Lithography 42
4.1.1 Photonic Forces 44
4.1.2 The Marangoni/Thermocapillary Effect 45
4.2 Characterization of the Marangoni Effect 46
4.2.1 Temporal Evolution of the Marangoni Effect 46
4.2.2 Power Dependence 49
4.2.3 Dependence on Film Thickness 50
4.2.4 Discussion of Observed Behaviour 51
4.2.5 Significance of the Interference Effect:
Experimental Verification 53
4.3 Feedback Mode and Constant Absorbed Power 56
4.3.1 Temporal Evolution of the Marangoni Effect:
Feedback Mode 56
4.4 High Laser Power 57
4.5 Block Copolymer Phases 60

4.6 Snow Plough Effect 63
4.7 Dewetting Enhanced Lithography 65
4.7.1 Rayleigh Instabilities of Thin Ribbons 65

5 Applications of the Marangoni Effect **68**
5.1 Micro-Optics Array 68
5.2 Microfluidic Devices 70
5.3 Additional Patterns 72

6 Conclusions **74**

References **76**

Appendices **79**
A Photonic Pressure 80
B Lensing Effect 82

List of Figures

1.1 Schematic of Poiseuille flow 3
1.2 Plot of the temperature dependence of the viscosity for PS 5
1.3 Glass transition temperature vs. crystallization temperature 6
1.4 Cohesive forces of the surface vs. bulk 7
1.5 The surface tension of a membrane 8
1.6 Depiction of the Marangoni effect 9

2.1 Lithography apparatus 13
2.2 Beam focusing 16

2.3 Beam alignment 18
2.4 Power meter calibration procedure schematic 21
2.5 Power meter calibration plot 22

3.1 Schematic of the heat equation problem 26
3.2 Plot of the calculated temperature distributions, various powers 35
3.3 Plot of the calculated temperature gradients 36
3.4 Plot of the reflectance of a PS film on Si 39
3.5 Plot of the calculated temperature rise vs. film thickness 39
3.6 Optical microscope image of PEO temperature calibration 41

4.1 AFM image of laser trenches and holes 43
4.2 AFM cross section of a laser hole 44
4.3 Optical image of a series of holes with increasing irradiation time 46
4.4 AFM cross section of a hole evolution 48
4.5 Maximum hole depth of a time evolution—Power dependence 49
4.6 Maximum hole depth of a time evolution—Film thickness dependence 50
4.7 Remaining film thickness vs. time for a series of hole evolutions 51
4.8 Plot of the reflectance as a function of film thickness 52
4.9 Optical microscope image of a laser formed thickness gradient 53
4.10 Reflected power vs position for Fig. 4.9 54
4.11 Close inspection of reflected power vs. position plot 54
4.12 Measured reflected power over the time of two hole evolutions 55
4.13 Plot comparing the reflected power behaviour to the measured hole depth . 56
4.14 Maximum hole depth as a function of time—Feedback Mode 57

4.15 AFM image of a high power laser formed hole 58
4.16 AFM cross sections of a high power hole evolution 59
4.17 Schematic of block copolymer surface morphology 60
4.18 AFM image of ordered block copolymer films 61
4.19 Assortment of laser patterned films—Block copolymers 62
4.20 The snow plough effect 63
4.21 Incomplete removal of film 64
4.22 Thin ribbons dewetting into ordered droplets 66
4.23 Patterned film dewetting into constrained structures 67

5.1 Microlens array 69
5.2 Dewetting of a square film into a droplet (schematic) 70
5.3 Microfluidic reservoir and 'Y' channel 71
5.4 Spiral patterns in a PS film 72

5.5 Assortment of patterns 72
5.6 Salute to Canadian athletes 73

List of Tables

2.1 Specifications for the Verdi V-2 Laser System 14
2.2 Mitutoyo NIR 10 x Objective Specifications 16

3.1 Optical and Physical Properties of Selected Materials 27

Chapter 1

Introduction

Laser technology readily lends itself to a broad spectrum of applications within the field of materials processing, offering the unique properties of laser radiation as a tool for material removal and ablation, material deposition and growth, material transformation and synthesis and, the topic of this thesis, lithographic patterning.

The largest motivation for this particular project draws from the capacity to generate extremely sharp and localized temperature gradients with a tightly focused continuous wave (*cw*) laser beam on the surface of thin polymer films. Quantitatively, thermal gradients exceeding 1,500,000 °C/cm are easily accessed and spatially controlled with sub-micron precision enabling the direct patterning of films with micron and nanometre scale resolution. While the procedure discussed in this thesis is not suitable for mass production owing to the limited writing speed, the presented lithography system enables an extremely rapid prototyping turnaround, where novel 3-D patterns can be quickly imprinted into a sample, drastically reducing the minimum time from initial concept to finished product as compared to conventional pattern transfer techniques [1-2]. Over recent years, thin polymer film temperature phenomena such as dewetting [3], crystallization [4], self-assembly [5] etc., have been the subject of thorough scientific study, however very few have examined the behaviour of these same material systems under the severe conditions of focused *cw* laser irradiation.

This introductory chapter begins with a brief review of the important photonic/material interactions that are often encountered during material laser processing followed by a more detailed examination of the relevant material properties and physics that will be drawn upon in subsequent chapters.

1.1 Laser/Matter Interactions

Focused laser radiation can interact with a material through a number of different mechanisms that are determined by the physical and chemical properties of the materials, as well as the characteristics of the laser irradiation. Important physical parameters include the dielectric constant, thermal conductivity and mass density which govern the propagation and absorption of light and heat within a material. The specific chemical composition and microstructure of a material determine the elementary excitations and behaviours responsible for the mechanism. Noteworthy laser parameters include the incident power and beam waist, the wavelength, polarization, angle of incidence and the irradiation time.

Depending upon the chosen combination of materials and laser parameters, photonic interactions can vary from simple reflection/refraction to highly destructive material vaporization. The most important interaction concerning laser lithography is the generation of a local thermal gradient.

1.2 Physics and Material Properties of Polymers

Polymers are a class of *macromolecules* that are composed of a large number of repeating units, or *monomers*, joined by covalent bonds to form long chain structures. Owing to their unique chemical structure, polymeric materials exhibit an incredible assortment of physical and mechanical properties ranging from simple Newtonian viscous behaviour to complex viscoelastic properties [6]. While studying the properties of these materials is not the goal of this thesis, it will prove instrumental to first briefly examine the polymer concepts and properties most relevant to the work that will be subsequently presented. With the most prevalent laser/matter interaction of the lithography process being an induced temperature rise, the thermal dependencies of these properties will be brought into focus.

1.2.1 Viscosity

When characterizing the flow behaviour of a liquid, one of the most important rheological properties is the *viscosity,* which is a measurement of a fluid's resistance to flow. For a Newtonian fluid in motion, the velocity of the moving liquid, scaled by the thickness of the fluid layer, is proportional to the shear force *F* per unit area *A* (see Fig. 1.1). The proportionality constant linking the relations is defined as the viscosity, η [7]:

$$\tau = \eta \cdot \frac{v}{h}; \tag{1.1}$$

where τ is the shearing stress or force *F* per unit area *A*, *v* is the tangential velocity of the flow and *h* the thickness of the fluid layer.

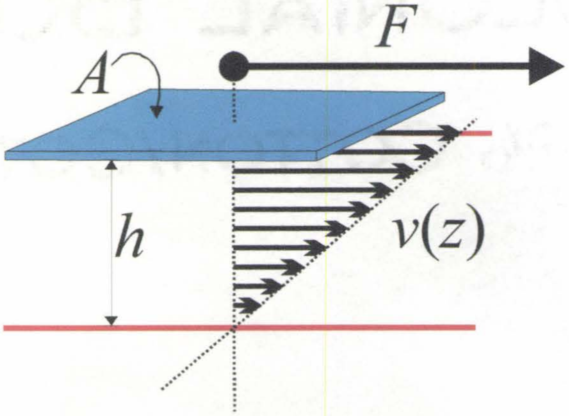

Figure 1.1: The velocity field *v*(*z*) generated by the application of a shearing force *F* to the surface of a liquid. The illustrated velocity profile corresponds to Poiseuille (or laminar) flow, where the velocity field monotonically reduces to zero at the lower (solid) boundary interface.

The majority of liquid polymer melts exhibit two regimes of flow behaviour: *Newtonian* and *shear thinning.* Newtonian (also referred to as laminar) flow occurs for low shear stresses where the viscosity describing the fluid remains constant and independent of the shear rate. For higher shearing rates, the macromolecules of the system begin to disentangle and align allowing the giant molecules to slide past one another with a reduced resistance to flow; this behaviour is classified as shear thinning [8]. Additionally, the viscosity of polymer melts can vary by many orders of magnitude with a changing temperature. The thermal gradients introduced by the focused beam of the lithography system necessitate a closer examination of the temperature/viscosity dependency.

1.2.1.1 Viscosity—Temperature Dependence: The WLF Equation

The temperature dependency of the viscosity $\eta(T)$ is best described by the empirical relation proposed by William, Landel and Ferry, known as the 'WLF equation' [8]. With knowledge of the viscosity at some reference temperature, T_o, we can calculate the new viscosity at any temperature with the following relation:

$$\log\frac{\eta_o(T)}{\eta_o(T_o)} = -\frac{C_1\left(T-T_o\right)}{C_2+\left(T-T_o\right)}; \tag{1.2}$$

where $\eta(T)$ is the shear viscosity at temperature T, T_o is the chosen reference temperature and C_1 and C_2 are characteristic constants of the polymer material.

In most cases one chooses the glass transition temperature, T_g, as the reference temperature and the WLF constants C_1 and C_2 can be found in many sources [9-10]. For polystyrene (PS), the constants are $C_1 = 14.63$ and $C_2 = 60$ and $T_g = 371$ K. In Figure 1.2 we plot the viscosity as a function of the temperature normalized to the reference viscosity.

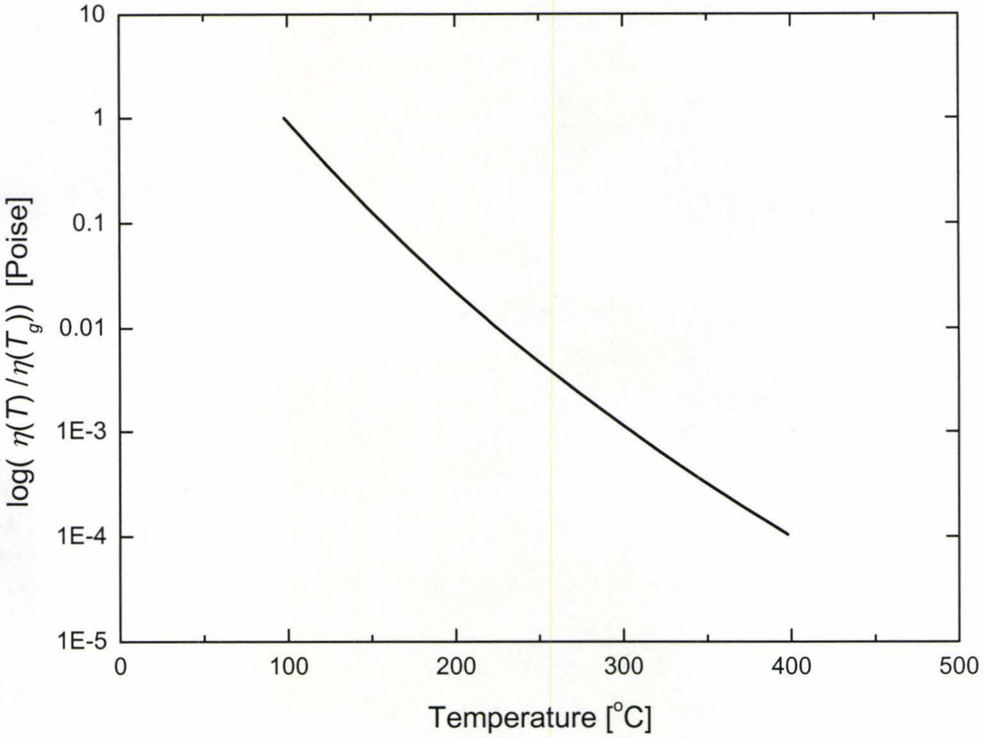

Figure 1.2: Temperature dependency of the viscosity $\eta(T)$ (normalized to $\eta(T_g)$) for PS as predicted by the WLF equation. The viscosity is seen to vary by several orders of magnitude over a typical range of temperatures accessible by *cw* laser irradiation.

1.2.2 Polymer Glass Transition

The glass transition temperature is a very important material parameter that marks the phase boundary between the liquid or *melt* state of a polymer material and that of a disordered solid or *glass*. Its existence can be understood by considering the physical structure of a polymer, where the long entangled macromolecular chains ultimately govern its behaviour. Consider, for example, what happens when we quickly cool a polymer melt to a temperature at which a crystalline conformation is most favourable: The strong temperature dependence of the viscosity increasingly hinders the movement of the constituent molecules to the point where they are essentially frozen in place, locking in the random molecular conformations characteristic of a liquid melt [8].

A more quantitative description of the liquid to glass transition is depicted schematically in Figure 1.3. In cooling an amorphous (polymer) material from the liquid state, we see a smooth change in volume as it solidifies (1). Note that the intersection of the two straight segments defines the glass transition temperature (Tg). This is in contrast to the behaviour of a cooling crystalline material (2) in which we observe a very sharp change in volume it passes through its crystallization temperature (Tc).

The specific value of the glass transition temperature depends on chemical structure, molecular weight and on the rate of cooling.

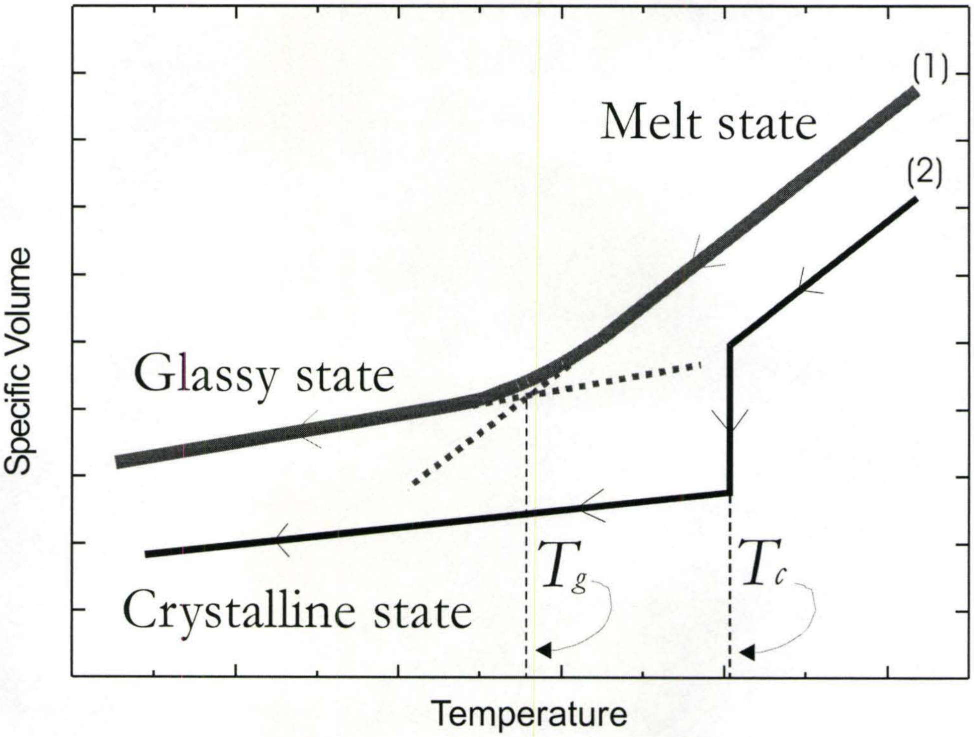

Figure 1.3: Comparison of the transitions between the melt and solid state for a glassy material (1) and a crystalline material (2).

1.2.3 Surface Tension

Surface and interfacial effects are of great interest to the scientific community as properties at interfaces often differ from the bulk. A perfect example of this phenomenon is *surface tension* whose origin stems from the balance of cohesive forces between the molecules and atoms of a liquid system [11]. Consider Figure 1.4 that depicts the molecular basis for the surface tension by examining the attractive forces that exist between the molecules of a liquid. Within the bulk of a material, the surrounding molecules attract each other equally in all directions, leading to a balanced net force of zero. The picture is slightly different for a molecule located at the surface, where the absence of similar atoms above the interface leads to an asymmetry in the intermolecular forces and a net attraction towards the interior of the liquid medium. The net cohesive forces cause the liquid surface to contract until a balance with the repulsive collisional forces of the other molecules is reached.

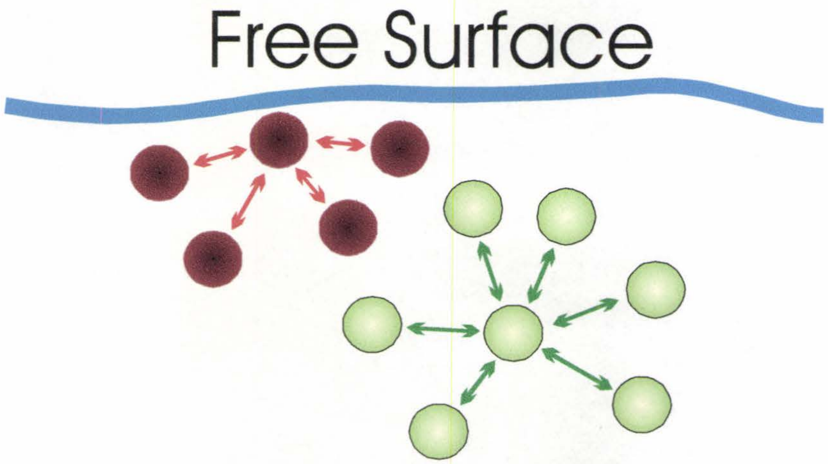

Figure 1.4: Cohesive force balancing within the bulk (light green) and surface (dark red). The absence of interactions above the free surface results in a net downward force exerted on the surface atoms.

Quantitatively, the surface tension (γ) is measured as a force (F) per unit length (l) as described by the geometry of Figure 1.5. The surface of a liquid behaves like a taut membrane that will resist stretching by an external force due to cohesive forces between the constituent atoms.

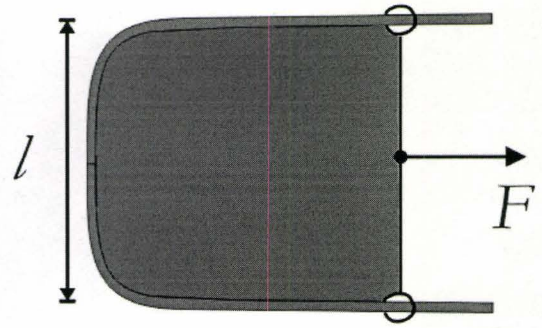

$$\gamma = \frac{F}{2l} \tag{1.3}$$

Figure 1.5: Illustration of a thin membrane (for example, a soap film) between a wire grid. The surface tension is a measure of the cohesive forces binding the atoms on the surface of a liquid. The surface tension can be determined by measuring the force required to equilibrate the cohesion forces of the surface atoms. A factor of $2l$ enters in (1.3) because the suspended film has two surfaces.

The strength of the surface tension changes with the polymer's chemical composition and, of great importance for laser processing, with temperature. As with many materials, a rise in temperature decreases the surface tension due to a decrease in the intermolecular binding forces. For PS, the surface tension decreases by 0.072 dyne/cm/°C, as measured by S. Wu [12].

1.2.4 The Marangoni/Thermocapillary Effect

When the focused laser beam of the lithography system interacts with a sample, it locally raises the temperature of the film. The density variance with temperature and subsequent buoyancy imbalance is the cause of convective fluid motion in heated systems. However, for thin films, the depth of the molten region (~ film thickness h) is typically smaller than the capillary length (l_{cap}), which is the distance over which interfacial tensions (and adhesion to surfaces→i.e capillary forces) remain important and is defined as $h < l_{cap} \approx \sqrt{\gamma / g\rho}$, where g is the acceleration of gravity on a body of density ρ [11]. As a consequence, the thermal dependency of the surface tension overpowers any effects caused by local density gradients.

In the section 1.2.3 we saw that the surface tension—an interfacial force per unit length—is a material parameter that typically decreases with temperature. We should therefore expect the thermal gradients introduced by the focused laser beam to cause a gradient in the surface tension. This effect is illustrated in Figure 1.6. The Gaussian intensity distribution of the focused beam generates a matching thermal profile on the surface of the thin film, with the maximum temperature rise located at the center of the irradiation region. This in turn creates a surface tension with a local minimum that smoothly increases radially outward from the center of the beam focus.

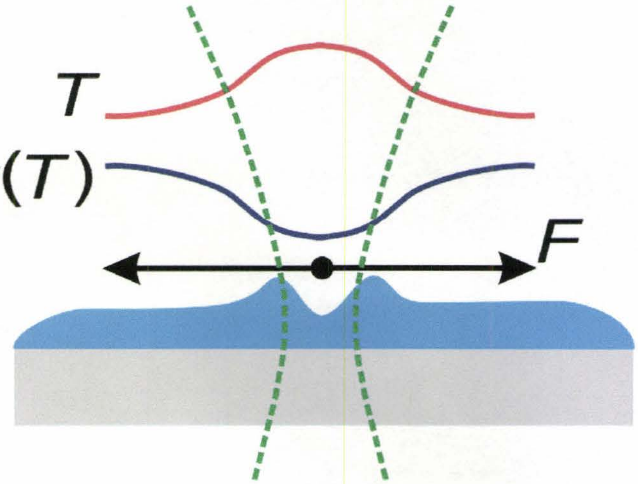

Figure 1.6: Illustration of the temperature profile (T) and the surface tension profile $\gamma(T)$ generated by a focused *cw* laser beam onto a thin polymer film.

The imbalance in surface tension gives rise to forces and liquid flow from the region of lowered tension to that of higher. This hydrodynamic phenomenon is called the Marangoni effect or more specifically, the thermocapillary effect when the source of the surface tension gradient is thermal [13].

A complete mathematical description of the behaviour of fluid flow arising from the thermocapillary effect requires the consideration of the Navier-Stokes equations [14]. However, insight into the phenomenon is possible with a simple model, which is sufficient for explaining the relevant physics. Assuming a linear (Newtonian) regime (i.e. constant viscosity), the viscous stress is related to the liquid flow through equation (1.1):

$$\tau = \frac{F}{A} = \eta \cdot \frac{v}{h};$$

The lateral gradient in the surface tension ($\nabla\gamma$) is the force F acting on an area A, therefore:

$$\nabla\gamma \sim \eta \frac{v}{h}. \tag{1.4}$$

The surface tension gradient can be written as:

$$\nabla\gamma = \frac{\partial\gamma}{\partial r} = \frac{\partial\gamma}{\partial T} \cdot \frac{\partial T}{\partial r}, \tag{1.5}$$

where $\partial\gamma/\partial T$ is the temperature dependence of the surface tension and $\partial T/\partial r$ is the thermal gradient caused by the focused laser beam.

Thus with some knowledge of the thermal distribution generated by the focused laser beam as well as a quantitative understanding of how the surface tension scales with temperature, the flow behaviour of a thin liquid polymer film under laser irradiation can be estimated.

1.3 Thesis Overview

The remainder of the thesis will be presented as follows:

Chapter 2 is a thorough description of the laser lithography system, including details of its calibration and operation, followed by an overview of the thin film preparation methods.

Chapter 3 examines the non-linear heat equation modelled for the interaction of laser light with a thin polymer film. An approximate solution to the equation is presented that describes the induced temperature profile across the sample surface. Optical interference effects have been found to significantly affect the temperature profile and are examined.

Chapter 4 studies in detail the driving mechanism of the lithography process: The Marangoni effect. The remainder of the chapter briefly discusses some preliminary work on high laser powers, different material systems as well as other thin film phenomena.

Chapter 5 is a brief description of some of the potential applications for the lithography system which include the fabrication of a micro-optic array and microfluidic devices.

The thesis concludes with a summary in Chapter 6.

Chapter 2

Experimental Apparatus

Comprised of only a few 'off-the-shelf' optical and mechanical components, the presented lithography system offers a relatively inexpensive method to precise attain spatial control over the sharp thermal gradients generated by a focused laser beam. The technology has demonstrated a very rapid prototyping turnaround, where novel 3-D patterns can be quickly imprinted into a sample, reducing the minimum time from initial conception to working prototype as compared to many traditional photolithographic techniques.

This chapter begins with a general overview of the apparatus followed by a detailed description of the basic components and features of the laser lithography system. The remaining sections present a comprehensive outline of the calibration and operating procedures (beam alignment, focusing and power calibration) and will conclude with details of the sample preparation methods.

2.1 General Overview of the Laser Lithography System

As shown in Figure 2.1, the beam from a variable power, *cw* laser is passed through a computer controlled, external high speed shutter and guided to the main assembly with a series of broadband metallic mirrors. The beam is directed up off the optical table with optics mounted onto a vertical breadboard, and then brought down towards the irradiation zone. Two irises, used for beam alignment, are mounted directly above the centerline of a long working distance microscope objective that tightly focuses the beam onto the sample surface. A sample holder is securely mounted to two computer controlled *x-y* translation stages, which are used to control the lateral position of the irradiation spot on the surface of the sample to be patterned. Light reflected off of the sample surface is re-collimated through the microscope objective and (1) used to focus the laser beam to a consistent spot size and (2) collected by a power meter in order to monitor the light intensity being absorbed by the sample.

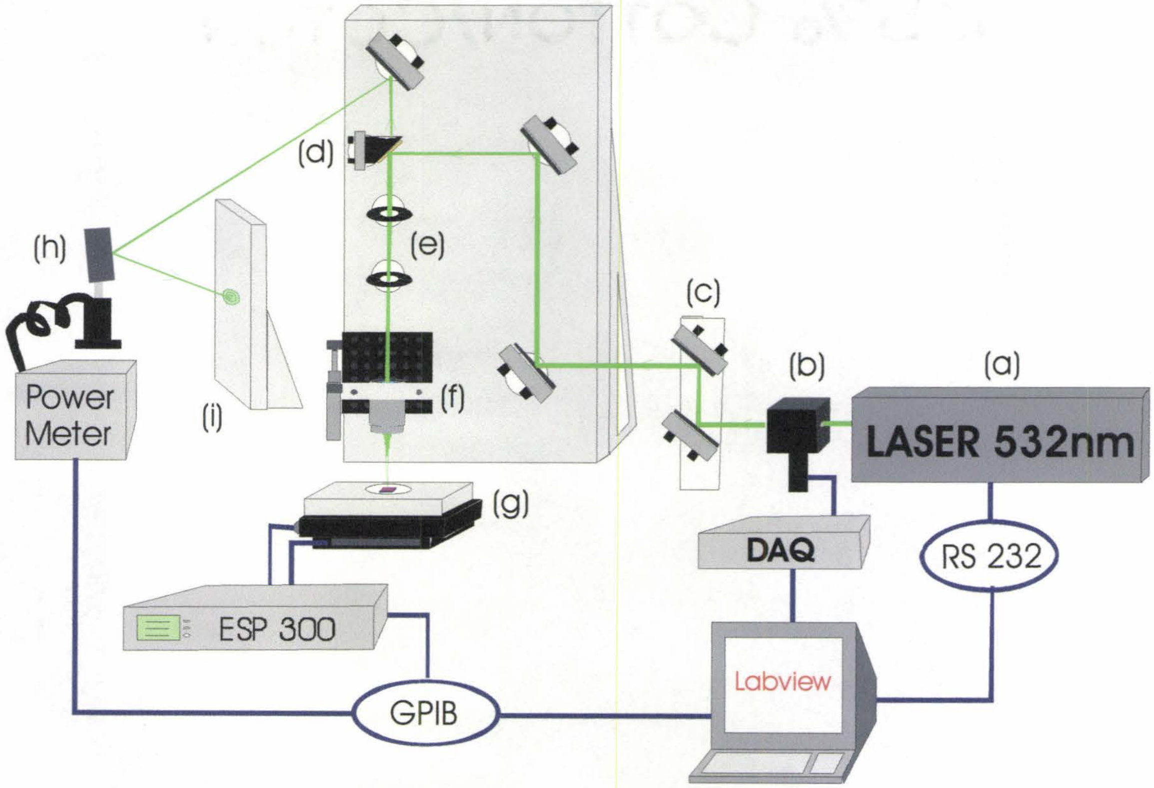

Figure 2.1: Schematic of the laser lithography system. The various components are (a) laser, (b) external shutter, (c) periscope assembly, (d) tuned dielectric mirror, (e) iris pair, (f) objective, (g) sample mount and *x-y* translation stages, (h) power meter, (i) focus viewing screen.

2.1.1 Laser System

The light source for the lithography system is a Verdi^{TM} V-2 (2.20 W) *cw* laser manufactured by Coherent. The package consists of a power supply and separate laser head that are connected by an optical umbilical cable. The power supply houses a compact solid-state diode laser which is used to pump, through the umbilical, a Nd:Vanadate (Nd:YVO_4) crystal located in the laser head. Output from the Vanadate gain medium is frequency doubled by a LBO doubling crystal, which is maintained at approximately 148 °C during operation. The resulting light output is a variable intensity, continuous wave, single frequency green (532 nm) beam with a nominal maximum power of 2.20 Watts. The laser head is securely mounted onto a water-cooled metal heat sink to maintain thermal stability. All of the various controlling parameters of the laser (power level, laser shutter, standby mode etc.) are computer controlled via a serial RS-232 computer connection. Table 2.1 lists the important laser specifications for the Verdi^{TM} V-2.

Table 2.1: Specifications for the Verdi^{TM} V-2 Laser System [15]:

Laser Parameter	**Specification**
Output Power	0 – 2.2 Watts *cw*
Output Wavelength	532 nm
Beam Diameter ($1/e^2$)	2.25 mm ± 10 %
Full-Angle Beam Divergence	0.35 mrad ± 10 %
M^2	< 1.1
Power Stability	± 1 %
Noise	< .02 % rms
Polarization	>100:1 vertical, linear
Linewidth	< 5 MHz rms
Pointing Stability	< 5 μrad/°C

2.1.2 External Shutter

Irradiation times for the experiments are controlled via a high speed, Newport 846HP shutter that is placed in front of the laser's output facet. The shutter's open/close state is computer controlled with a National Instruments DAQ board. While the Verdi$^{\text{TM}}$ V-2 contains its own internal shutter, the on/off response time of the 846HP (~10 ms) is significantly faster and more reliable for short timing experiments.

2.1.3 Optics Assembly

The laser beam is guided to the sample region by a series of standard broadband metallic mirrors, mounted to the optical table and vertical breadboard. The periscope assembly (Fig. 2.1 (c)) is not crucial to the lithography setup but is in place to accommodate the height of other experiments running simultaneously on the optical table. The mirror located at position (d) in Fig. 2.1 is a specially 'tuned' dielectric mirror with a transparent backing through which light reflected from the sample surface can be monitored to (1) focus the incoming beam to a consistent spot size and (2) monitor and control the laser power being absorbed by the sample. Two iris diaphragms are mounted along the optical axis of the microscope objective in order to verify and assist with beam alignment and sample levelling.

2.1.4 Objective

The laser beam is focused onto the sample through a Mitutoyo NIR 10 x long working distance objective. The optic is mounted onto a linear translation stage whose vertical position is manually controlled with a micrometer actuator to fine tune the focus.

Table 2.2: Mitutoyo NIR 10 x Objective Specifications [16]:

Objective Parameter	Specification
Numerical Aperture	0.26
Working Distance	30.5 mm
Focal Length	20.0 mm
Resolution Power	1.1 μm
Depth of focus	4.1 μm

Given the information presented in Tables 2.1 and 2.2, we can estimate the minimum spot size of the laser at the beam focus. For a $1/e^2$ beam diameter of 2.25 mm ± 10 %, the minimum attainable spot size ω_{02} with a 20.0 mm focal length f objective and 532 nm *cw* laser beam is given by [17]:

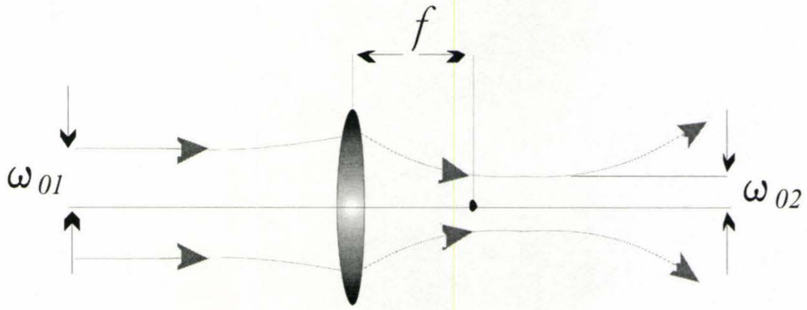

Figure 2.2: Definition of the important parameters that determine the minimum achievable spot size of a focused laser beam.

$$\omega_{02} \cong \frac{f \cdot \lambda}{\pi \cdot \omega_{01}} = \frac{20.0 \times 10^{-3} \cdot 532 \times 10^{-9}}{\pi \cdot \left(2.25 \times 10^{-3} \cdot \frac{1}{2}\right)} = 3.02 \times 10^{-6} \text{ m} \qquad (2.1)$$

Thus with the current optical setup, the laser beam can be focused to a theoretical minimum spot radius of ~ 3 μm.

2.1.5 Sample Mount

Samples to be patterned are placed at the beam focus on a compact Linkam^{TM} THMS 600 heating stage which can control the temperature of the substrate to a precision of 0.1 °C. This stage is mounted onto a two-axis tilt stage, which is used to ensure that the sample surface lies perfectly perpendicular to the incoming beam.

2.1.6 Translation Stages

The sample mount and tilt stage are secured to two one-axis translation stages that are actuated by separate Newport CMA-25CCCL linear drives. The motion of these stages is controlled by a two axis Newport ESP300 controller with a GPIB computer interface.

2.1.7 Power Meter

Light reflected off of the sample surface is re-collimated as it passes back up through the microscope objective and returns along the path from which it came. Owing to the transparent backing of the dielectric mirror (Fig. 2.1 (d)), a small fraction of this light leaks out and is collected by a Newport 1830-C Optical Power meter with a 818-SL photodetector. With a proper calibration (section 2.2.4), this fraction can be used to estimate the true reflected power and monitor the power being absorbed by the sample material.

2.1.8 Computer Control

Various components of the lithography system are controlled remotely through a standard Windows PC running Labview 6.1 enabling the control over the irradiation time, laser power and sample position while simultaneously monitoring and recording the absorbed laser power. All of the capable functions of the laser are accessed through an RS-232 serial communications link. The external shutter is interfaced with a data acquisition board. The ESP300 motion controller, which regulates the position of the translation stages, shares a GPIB interface with the optical power meter.

2.2 Calibration and Operating Procedures

The following section outlines the various procedures and techniques used during the operation of the lithography system. This includes laser beam alignment, sample levelling, beam focusing and power meter calibration.

2.2.1 Alignment Procedure

Ensuring that the laser beam is perfectly perpendicular to, and centered on, the entrance aperture of the microscope objective is necessary in order to maintain the symmetric profile of the incident laser beam through the focusing optics. While good, rectilinear alignment along the entire length of the beam path is good scientific practice, critical alignment occurs only at the last two mirrors. With the adjustments of mirrors (A) & (B), the beam can be steered through the exact center of each iris, marking the condition of a properly aligned system. The systematic procedure is as follows:

1. Close each of the iris openings to ~2-3 mm.
2. Use the controls of mirror (A) to center the beam through iris (1).
3. Use the controls of mirror (B) to center the beam through iris (2).
4. Re-iterate steps 2 & 3 until the beam passes through the center of both irises.

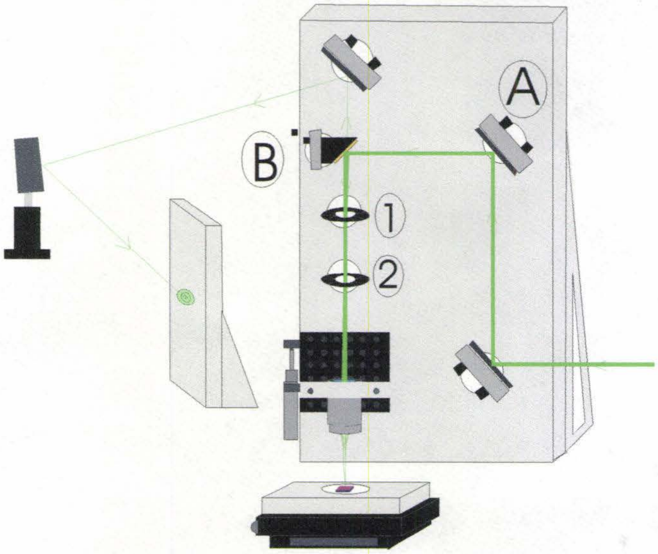

Figure 2.3: Simplified schematic of the lithography system

2.2.2 Focusing Procedure

It will be shown in Chapter 3 that the temperature rise induced by an incident laser is crucially dependent upon the width of the beam interacting with the surface. While this is a parameter that can be varied to regulate the induced thermal distribution, it would be challenging to reliably reproduce the exact conditions between experimental trials. Consequently, the beam is consistently focused to the same spot size.

Focusing the beam onto the sample is accomplished by adjusting the height of the objective with respect to the fixed sample surface. The light reflected from the sample surface is re-collimated as it passes back through the bottom face of the objective and returns along the path from which it came. A small fraction of this reflected light passes out the back of mirror (B) (in Fig. 2.3) and is directed towards the focus viewing screen. The spot size on the screen is focused by adjusting the height of the objective with respect to the sample surface until the smallest spot size is observed. To increase the accuracy of the procedure, the path length of the reflected light can be increased with additional mirrors.

2.2.3 Sample Levelling

Ensuring that the sample lies flat and perpendicular to the incident beam is necessary in order to maintain a constant focus and dependent thermal profile on the sample surface as it is laterally translated. Levelling is accomplished by adjusting a two-axis tilt stage that is fastened in between the sample holder and the two motorized *x-y* translation stages. The sample is judged to be level when the path from the reflected beam lies directly along the path of the incident beam. The levelling procedure is outlined as follows:

1. Referring to Figure 2.3, close iris (1) as much as possible while still allowing part of the incident beam to pass through. The beam will strike the sample and will be reflected back along the incident path.
2. By carefully looking up at where the reflected beam strikes the underside face of iris (1), adjust the tilt stage screws until it perfectly lines up with the hole through which it came.

2.2.4 Power Meter Characterizing Procedure

The optical power meter is in place in order to monitor the absolute value of the power being absorbed by the substrate, which is ultimately responsible for the thermal distribution that drives the lithography process. This is accomplished by measuring the reflected intensity and extracting the absorbed power from the conservation equation:

$$Laser\ Power = Absorbed + Reflected + Losses, \tag{2.2}$$

where *Laser Power* is the total light power exiting the laser cavity, *Absorbed* is the absorbed power into the sample, *Reflected* is the measured power from the sample surface and *Losses* is the remainder of the power dissipated through the various loss mechanisms. These losses include absorption and scattering by the guiding optics and laboratory environment, scattering of light from the sample surface that does not return along the original optical path etc.

The reflected light intensity that leaks through the dielectric mirror (Fig. 2.1 (d)) represents only a small fraction of the absolute reflected power. As a result, *Reflected* in equation (2.2) requires a correctional factor to compensate for this discrepancy and convert it to the actual reflected power:

$$Reflected \rightarrow Reflected^*; \tag{2.3}$$

where

$$Reflected^* = \frac{Measured\ Reflected}{Correction\ Factor}. \tag{2.4}$$

The method for determining this *Correction Factor* is shown schematically in Figure 2.4.

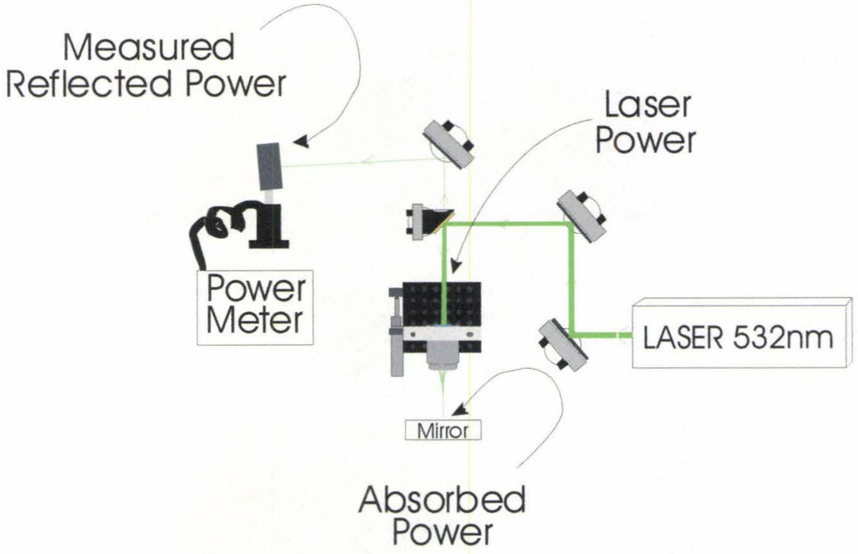

Figure 2.4: Schematic outlining the procedure for determining the *Correction Factor* of equation (2.4).

In place of a real sample, a reflective mirror is positioned under the objective at the beam focus and levelled following the procedures outlined in the previous section. Approximating the mirror as a near perfect reflector (Reflectivity > 99%), we can reasonably assume that the *Absorbed* component in (2.2) can be neglected. We can also accommodate for the *Losses* if the initial *Laser Power* is recorded at the entrance aperture of the objective, instead of from the output facet of the laser head. Providing that the mirror is carefully cleaned and levelled perpendicular to the beam, we can assume that all of the light focused onto the mirror returns back along the optical axis of the objective, ignoring scattering losses from the mirror surface. Equation (2.2) now simplifies to:

$$Laser\ Power = \frac{Measured\ R}{Correction\ Factor}. \tag{1.10}$$

By systematically recording and plotting the measured reflected power as a function of the incident laser power, the *Correction Factor* can then be determined from the slope of the interpolated trend line. A sample of such a plot is shown in Figure 2.5.

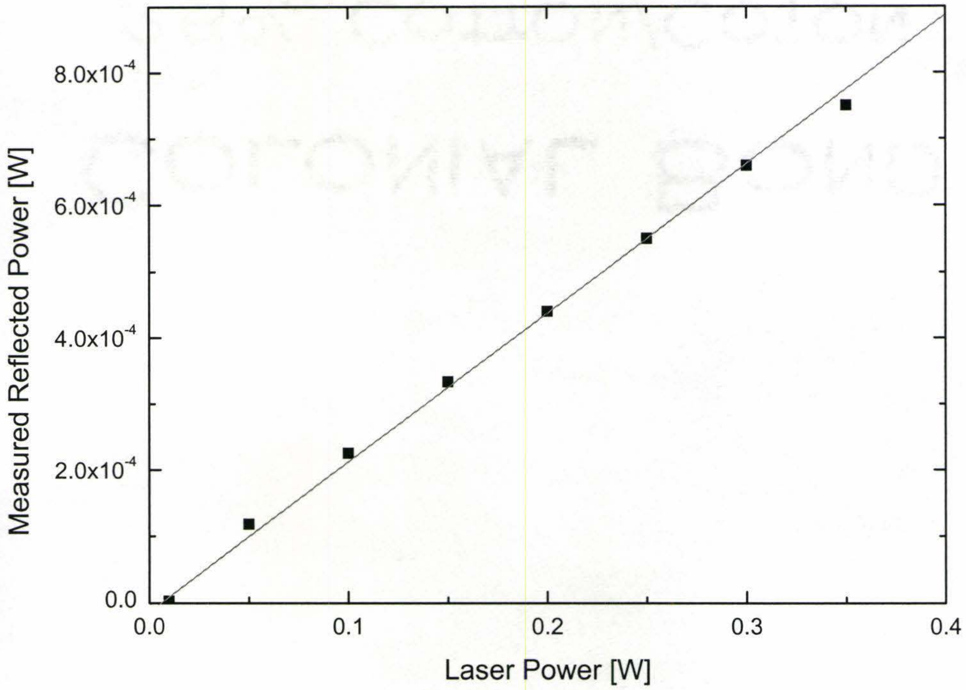

Figure 2.5: Sample calibration plot for determining the *Correction Factor* of equation (2.2). The value of the constant is simply the slope of the trend line. For this particular calibration, the slope is 0.0022546.

2.2.5 Feedback Mode (FM)

It will be shown in Chapters 3 and 4 that the thickness of the polymer film coating the substrate has a significant effect on the reflectivity (and absorption) of the sample material; Samples with different film thicknesses absorb differing amounts of light for the same incident laser powers. Additional complications arise during the lithography process itself, where patterning introduces local film variations with time, dynamically changing the absorbed laser power over the course of the experiment or trial.

To compensate for this potential problem, a dynamic PID feedback control loop has been developed in order to maintain the absorbed power entering the sample (and associated temperature distribution) at a constant level throughout the process and between samples. The main concept of the program is based on the conservation of laser power around the system:

$$Absorbed = Reflected * - Laser\ Power\,. \tag{2.6}$$

Setting the *Absorbed* power as the set point in the PID, the corrected reflected power (*Reflected**) is measured by the calibrated power meter. In order to keep the right side of (2.6) equal to the left side, the laser power simply has to increase with *Reflected**. The effectiveness of the program to maintain a consistent temperature distribution between samples of differing initial thickness was successfully proven with the temperature calibration described in Chapter 3, Section 3.6.

2.3 Sample Preparation

A typical sample that is patterned by the lithography system in this thesis is comprised of a thin ($100 \text{ nm} < h < 1000 \text{ nm}$) polymer film on a ~1 cm^2 piece of a carefully cleaned substrate. While not being limited to one particular film or substrate material, the samples examined in the work of this thesis are Poly(styrene) (PS), Poly(styrene)-b-Poly(methyl methacrylate) (PS-b-PMMA), Poly(ethylene oxide) (PEO), Poly(dimethylsiloxane) (PDMS) and PS on PDMS, all on silicon substrates.

General sample preparation is undertaken in 4 separate steps: *Solution preparation*, *substrate preparation*, *film deposition* and *post-annealing*. Each process will be described in detail.

2.3.1 Solution Preparation

The solutions used in this study are made by dissolving a carefully weighed amount of solid polymer into a filtered solvent and stirred for at least 12 hours to ensure complete mixing. Mass fractions and molecular weights vary from 1.00 to 3.00 % and 15,000 to 734,000 g/mol respectively, whose choice depends on the desired film thickness range. Toluene was used as the solvent for all polymers discussed except for PEO, which is dissolved in chloroform or acetonitrile.

2.3.2 Substrate Preparation

The most important detail of substrate preparation is cleanliness—dust particles and other contaminants present in a thin film can nucleate unwanted holes, and scatter and absorb light—disrupting the lithography process. To minimize these problems, a sequence of cleaning steps has been adopted for optimal film results.

Undoped, <1 0 0> silicon wafers are carefully cleaved into 1 cm^2 squares under a laminar flow hood and individually dusted with low pressure nitrogen gas. Placed on a heating stage set at ~150°C to minimize condensation, each silicon square is then cleaned with a CO_2 snow jet, which mildly ablates away oils, dust and other contaminants in a matter of seconds. The substrates are then placed in a BioForce Laboratory UV ozone chamber for 30 minutes in order to remove any residual organic contaminants. As final cleaning step before depositing a film, the substrate is placed on a Speedline Technologies spin coater and spun at high speed under the laminar flow hood. From separate pipettes, 10 drops of acetone, methanol and then toluene are each dropped (in that order) onto the spinning substrate.

2.3.3 Spin Coating

The thin films are prepared by depositing 2 to 3 drops of filtered polymer solution onto the substrate and immediately spinning it at high speed for 40 seconds. The final thickness of the film depends on the details of the polymer solution (molecular weight and concentration) as well as the spin speed and acceleration of the spin coater. The film thicknesses examined in this thesis, ranging typically from 100 to 500 nm, are obtained at full acceleration with spin speeds between 1000 and 5000 rpm.

2.3.4 Post Annealing

As a final preparation step, after spin coating, the films are placed under vacuum and heated to 130 °C for at least 12 hours in order to evaporate residual solvent molecules in the film and relax the polymer chains.

Chapter 3

Modelling of Processes

The following chapter investigates in detail the most important photonic/matter interaction of the laser lithography system described in this thesis: the laser induced temperature rise. The chapter begins with a thorough description of the problem, followed by a mathematical treatment and approximate solution of the modelled heat equation. The second section of this chapter outlines an experimental method for verifying the validity of the derived temperature expression and provides proof that it is in fact reasonable. The chapter concludes by exploring the influence of the polymer film coating the substrate and its ultimate effect on the temperature distribution.

3.1 Description of the Problem

Figure 3.1 is a pictorial representation of the laser/material problem. A 532 nm *cw* laser beam is focused onto the surface of a sample consisting of a thin polymer film, with heat conductivity (κ_f) and refractive index (n_f), coating a silicon substrate (κ_s, n_s). The bottom of the sample is in thermal contact with a controlled heat stage and held at a set temperature. Owing to the transparent nature of the polymer film, it is assumed that the focused beam passes through the first layer without interaction and is absorbed solely by the substrate, locally raising the interfacial temperature by an amount $\Delta T(x, y, z=-h, t)$. Heating of the polymer film occurs indirectly via conduction between the film and substrate interface. The dimension of the film thickness (h) is assumed to be small enough that the temperature rise and thermal profile on the surface of the polymer film closely matches that of the contacting silicon substrate.

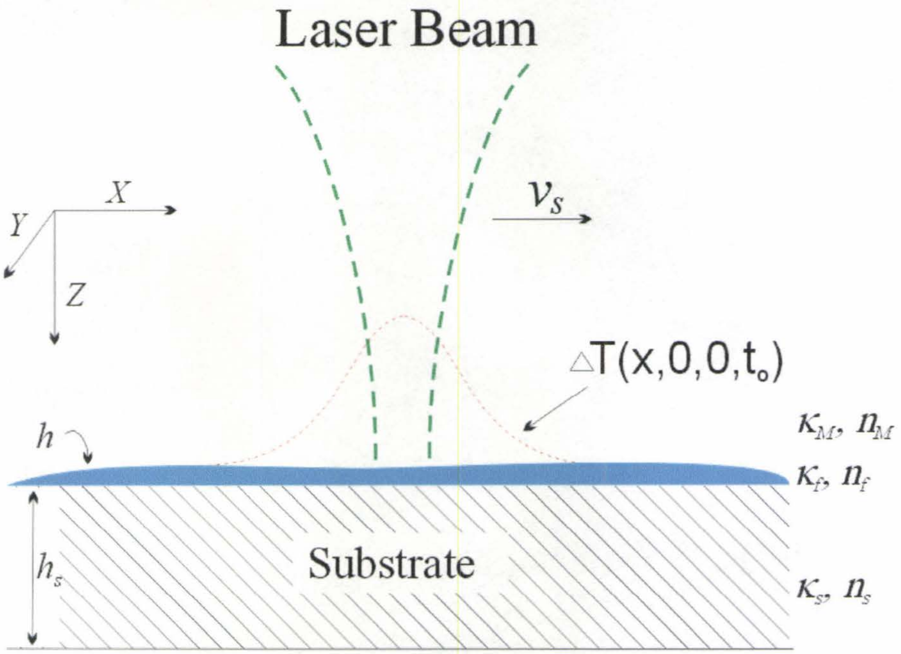

Figure 3.1: Schematic of the laser beam/material interaction problem. Film and substrate thicknesses (h_f and h_s), heat conductivities (κ_f and κ_s) and indices of refraction (n_f and n_s).

Table 3.1 summarizes some important optical and physical properties for the silicon substrate and various polymer materials. All values are quoted at $T = 300$ K and for a laser wavelength (λ) of 532 nm when applicable.

Table 3.1: Optical and Physical Properties of Selected Materials

	Si	**PS**	**PMMA**	**PEO**	**PDMS**
Index of Refraction, n	4.142	1.512	1.49	1.477	1.490
Absorption Coefficient, α [cm^{-1}]	5.0 x 10^3	*Transparent*			
Thermal Conductivity, κ [W / mK]	156	0.105	0.21	0.42	0.25
Specific Heat @ Const. pressure, c_p [J/gK]*	0.71	0.454	0.574	55.36**	0.713
Melting (Glass) Temperature, T_m or T_g [°C]	1416	100	105	68	-123

*Values taken near T_g for $M_W \sim 100$ g/mol.

**Units: J/molK

Polymer data obtained from [9-10] & [4]. Silicon data from [1].

3.2 The Heat Equation

The flow and transfer of energy from the focused laser beam into the substrate is governed by a differential heat equation, whose solution will provide the spatial temperature distribution induced by the laser. However, it should be noted that many of the quoted material properties in Table 3.1 exhibit strong temperature dependencies. Coupling these properties with a spatially varying thermal distribution leads to an inhomogeneous material system, which requires the consideration of the non-linear version of the heat equation, given by [1]:

$$\rho(T)\cdot c_p(T)\cdot\frac{\partial T(x,y,z,t)}{\partial t}-\nabla\left[\kappa(T)\cdot\nabla T(x,y,z,t)\right]+\rho(T)\cdot c_p(T)\cdot v_s\cdot\nabla T(x,y,z,t)=Q(x,y,z,t); \tag{3.1}$$

where $\rho(T)$ is the mass density of the irradiated material, $c_p(T)$ is the specific heat at constant pressure, $\kappa(T)$ is the thermal conductivity and v_s the relative velocity of the heat source with respect to the sample surface. $T(x,y,z,t)$ defines the temperature profile and $Q(x,y,z,t)$ the details of the heat source.

3.2.1 The Source Term Q(x,y,z,t)

Before proceeding with the solution to the non-linear heat equation, a full definition of the source term *Q(x,y,z,t)* is required. For the problem depicted in Figure 3.1, heating is caused by the absorption of light into the substrate material. The heating term for such a source can be generalized as follows:

$$Q(x,y,z,T) = I_o\left(1 - R(T,\lambda)\right)\cdot g(x,y)\cdot f(z)\cdot q(t)\,; \tag{3.2}$$

where we discuss each term, in turn, below.

3.2.1a Absorbed Intensity

$I_o(1\text{-}R(T,\lambda))$ = Maximum intensity absorbed by the surface. I_o is the total incident intensity, which is partially reflected depending upon the magnitude of the reflectance, given by $R(T,\lambda)$.

It is often preferred to speak of laser *power*, in place of *intensity*. For a symmetric, Gaussian source, the two are related through:

$$P_o = \pi\omega_o^2 I_o\,; \tag{3.3}$$

where ω_o is the radius of the laser focus defined by the convention $I(\omega_o) = I_o/e^2$, the point where the intensity has dropped to 86 % of its maximum value. P_o is the effective power that is incident onto the sample surface. It is referred to as *effective* since it takes into account all the losses and inefficiencies that arise from the components of the laser system and experimental setup.

The *reflectance* or *reflectivity* R, is dependent upon the indices of refraction of the interacting materials and is calculated by the Fresnel equations. A secondary component to the reflectivity arises from the physical structure of the sample. The thin polymer film sets up an etalon-like cavity, where interference effects can enhance or diminish the overall reflectivity of the sample surface—A topic that will be discussed in detail in section 3.5. For an uncoated substrate at normal incidence, the reflectivity is calculated by the following [18]:

$$R = \left(\frac{1 - n_S/n_M}{1 + n_S/n_M}\right)^2. \tag{3.4}$$

3.2.1b Spatial Profile

$g(x,y)$ = Spatial profile of the intensity on the irradiated surface.

The most common spatial profile has a Gaussian dependence, which has an intensity distribution within the focal plane described as:

$$I(r) = I_o \cdot \exp\left(-\frac{x^2+y^2}{\omega_o^2}\right) = \frac{P_o}{\pi\omega_o^2} \cdot \exp\left(-\frac{x^2+y^2}{\omega_o^2}\right). \tag{3.5}$$

3.2.1c Depth Profile

$f(z)$ = Depth attenuation function below the substrate surface.

If the interacting material is not a perfect dielectric (i.e. contains a complex component in the index of refraction), then absorption will occur—leading to the decay of light intensity as it passes through a material. The penetration depth (often characterized by the skin depth) has a significant effect on the profile and maximum temperature rise of the induced thermal distribution. The attenuation as a function of depth is given by:

$$f(z) = \alpha(T(z)) \cdot \exp\left(-\int_0^z \alpha(T(z))dz\right); \tag{3.6}$$

where $\alpha(T(z))$ is the temperature dependent absorption function, which in turn is dependent on the depth z. For crystalline silicon, the absorption coefficient ~$5.0\text{x}10^3$ cm^{-1} which corresponds to a skin depth of $1/\alpha \sim 20$ nm [18].

3.2.1d Time Dependency

$q(t)$ = Temporal dependence of the intensity or pulse shape

The instantaneous and accumulated exposure times of the laser radiation both play a role in the resultant temperature distribution and processing behaviours. This parameter becomes particularly important for pulsed or moving sources when certain processes occur on a time-scale faster than the thermalization time (τ), which is the time required for the system to approach steady state. For our system, we estimate τ to be at most a few microseconds [19]. Since our processing time is much greater than this, we can reasonably neglect any time dependency assuming that the temperature of the system has reached steady state.

3.2.1e The Complete Source Term…

Considering all of the above, the generalized source term for laser irradiation becomes:

$$Q(x,y,z,T) = \left[1 - R(T,\lambda)\right] \cdot \left(\frac{P_o}{\pi \omega_o^{\,2}} \right) \cdot \exp\left(-\frac{\sqrt{x^2 + y^2}}{\omega_o} \right)^2 \cdot \alpha(T(z)) \cdot \exp\left(-\int_0^z \alpha(T(z))dz \right). \tag{3.7}$$

3.2.2 Boundary Conditions

Solving the partial differential heat equation (3.1) requires the careful consideration of the system's boundary conditions. Taking Figure 3.1 as the model, we consider a semi-infinite substrate of that is irradiated by a tightly focused laser source. It is also assumed that the lateral dimensions are much larger than the beam waist ($l_x, l_y >> \omega_o$). For simplicity, the temperature rise on the surface of the film is assumed to be equivalent to the temperature rise of the bare substrate. This is a reasonable assumption owing to the scale of the film (h < 500 nm). This may not hold for thicker films where conduction may become more significant. Finally, we shall assume that the substrate is immersed in a gaseous medium M and that the temperature distribution is continuous across the boundary interfaces:

$$T_s\left(x,y,z=0,t\right) = T_M(x,y,z,t), \tag{3.8}$$

$$T_s\left(x,y,z=h_S,t\right) = \text{ Hot Plate Temperature}. \tag{3.9}$$

Accounting for the various energy fluxes in and out of the surfaces lead to another boundary condition. At the 'open air' interface:

$$-\kappa_s \frac{\partial T_s(x,t)}{\partial z} = \eta\left[T_s(x,y,0,t) + T_M(\infty)\right] + \sigma_r \varepsilon_t \left[T_s^4(x,y,0,t) - T_s^4(\infty)\right]; \tag{3.10}$$

where

$-\kappa_s \dfrac{\partial T_s(x,t)}{\partial z}$ is the entering energy flux into the substrate.

$\sigma_r \varepsilon_t \left[T_s^4(x,y,0,t) - T_s^4(\infty)\right]$ is the energy flux lost by thermal radiation.

The Stephan-Boltzmann constant is σ_r = 5.7 x 10^{-12} W/cm^{2}K^4. ϵ_t is the total emissivity. For polished Silicon, $\epsilon_t = 0.68$ [20].

$\eta\left[T_s(x,y,0,t)+T_M(\infty)\right]$ includes the convective losses into the ambient medium.

η is the coefficient of surface heat transfer which is dependent upon the relative values of κ_S and κ_M, the geometry of the substrate, the flow rate of the ambient medium etc. $T_M(\infty)$ is the unperturbed temperature of the ambient medium.

3.3 Calculation of the Induced Surface Temperature: Temperature Independent Parameters

Analytic expressions for the described boundary problem have been determined by Lax and others [21-24, 19] for stationary conditions and temperature independent material parameters. While numerical solutions have been proposed for the non-linear case, the analytic approximations provide us with better insight and intuition into the dependencies and interactions of the laser parameters and material system.

3.3.1 The Maximum Temperature Rise

One of the most significant parameters to calculate is the maximum temperature rise that the laser beam can induce. Knowledge of this value becomes particularly important if the processing mechanism depends upon some threshold temperature requirement or critical damage level. Naturally, the maximum temperature rise occurs in the region where the laser intensity is the highest. For a Gaussian laser source, this is located at the center of the beam profile. Ignoring all heat loses ($\eta = 0$) and allowing $\alpha \rightarrow \infty$, we obtain a central temperature rise (θ_c) for a Gaussian laser source from the following [21]:

$$\theta_c \equiv \Delta T_c(\alpha \to \infty, \eta = 0) = \frac{1}{2\sqrt{\pi}} \cdot \frac{P_o \cdot (1-R)}{\omega_o \cdot \kappa_S}. \tag{3.11}$$

3.3.2 Spatial Temperature Profile

The spatial profile of the laser induced temperature rise is first modeled for the simplest case: the condition where the absorption coefficient is very large ($\alpha \rightarrow \infty$). This situation is referred to as *surface absorption* where all of the laser power is absorbed in an infinitesimally small layer at the surface of the material. This removes the complexities of following the behavior of the heat fluxes into the bulk of the irradiated material. For additional simplicity, we will initially ignore the temperature dependencies of the absorption coefficient $\alpha = \alpha(T_o)$, thermal conductivity $\kappa = \kappa(T_o)$ and reflectivity $R = R(T_o)$, taking their values at a fixed temperature T_o. The effects of the temperature dependencies will be introduced later as a perturbation to the simplified profiles.

The radial temperature distribution within the surface plane of the sample, centered around the maximum temperature rise, can be approximated by [21]:

$$T(r, z=0) \approx \frac{\theta_c}{\sqrt{\left(1+r^2\right)}}. \tag{3.12}$$

The temperature rise into the bulk of the of the substrate follows:

$$T(r, z) \approx \frac{1}{\sqrt{\pi}} \cdot \frac{\theta_c}{\sqrt{\left(r^2+z^2\right)}}. \tag{3.13}$$

3.3.3 Finite Absorption

While the absorption coefficient of silicon is large ~ 5.0 x 10^3 cm^{-1} at a wavelength of 532 nm, it is certainly far from being infinite. We must therefore take into consideration the effect that a finite absorption layer might have on the distribution of the temperature within the substrate. Compared to the case of infinite absorption, we should expect an overall decrease in temperature with a decreasing absorption coefficient due to a reduction in the local power density. Treating the effect as a perturbation to equation (3.11) (infinite case), a finite absorption coefficient modifies the temperature by an amount [1]:

$$\Delta T(r=0, z=0; 0.1 \leq \alpha^* \leq 10) \approx 0.53 + 0.165 \ln\left(\alpha^*\right); \tag{3.14}$$

where α is scaled by ω_o according to $\alpha^* = \alpha\,\omega_o$.

The resulting central temperature rise $\theta_c(\alpha^*)$ is then:

$$\theta_c\left(\alpha^*\right) = \left[0.53 + 0.165 \ln\left(\alpha^*\right)\right] \times \theta_c(\alpha \to \infty). \tag{3.15}$$

3.4 Calculation of the Induced Surface Temperature: Temperature Dependent Parameters

A more realistic model takes into account the temperature sensitivity of material properties such as the thermal conductivity, reflectivity and absorption coefficient. The following section will examine and quantify the influence that such dependencies will have on the overall temperature distribution.

3.4.1 Thermal Conductivity

For crystalline semiconductors, such as silicon, the thermal conductivity is governed by phonon-phonon interactions [25] and decreases with increasing temperature. A decreased thermal conductivity will restrict heat dissipation and effectively enable a higher temperature rise in the region of irradiation. For silicon, including a temperature dependent thermal conductivity results in the __equation [24]:

$$T(T) = T_k + \left[T(\infty) - T_k\right] \cdot \exp\left(\frac{T}{T(\infty) - T_k}\right); \tag{3.16}$$

for 300 K < T < 1400 K, where $k = 299$ W/cm and $T_k = 99$ K.

3.4.2 Reflectivity

The reflectivity of a thin film system depends on a number of factors. It is sensitive to the interacting wavelength of light, the thickness of the coating layer and on the refractive index of the composing materials. For semiconductors, a complex dependence on temperature is observed and governed by the influence of thermally activated electrons. For silicon, at a temperature T, the reflectivity becomes [27]:

$$R(\lambda, T) \approx R(\lambda, T_o) + 5 \times 10^{-5} T; \tag{3.17}$$

for $T < 1000$ K and $\lambda > 410$ nm. Thus an increase in temperature corresponds to an overall increase in the reflectivity of the substrate. For a constant irradiation power, the increase in reflectivity lowers the amount of power being absorbed into the material, which reduces the overall temperature rise.

3.4.3 Absorption Coefficient

For semiconductors, the strength of the absorption coefficient comes primarily from contributions of both interband and free carrier absorption, the latter of the two being extremely sensitive to thermal fluctuations. Experimental data for the temperature dependence of the absorption coefficient for crystalline silicon follows the approximate relationship [27]:

$$\alpha(T) \approx \alpha_o \exp\left(\frac{T}{T_R}\right). \tag{3.18}$$

This is valid for wavelengths greater than $\lambda > 410$ nm and temperatures within the range $300\text{ K} \leq T \leq 1000\text{ K}$. Where $\alpha_o = 5.0 \times 10^3\ \text{cm}^{-1}$ at 532 nm and $T_R = 430$ K.

3.4.4 The Final Picture

Combining all of these effects together, we end up with an approximate surface temperature profile described by:

$$T(r) \approx \cdot \left\{ \left(T_k + \left(T_{sub} - T_k\right)\right) \cdot \exp\left[\frac{\left(0.53 + 0.165 \cdot \ln\left(\alpha_o \exp\left({}^{T}\!/_{T_R}\right)\right)\right) \dfrac{P_o \cdot \left(1 - \left(R(\lambda, T_o) + 5 \times 10^{-5} T\right)\right)}{2 \cdot \sqrt{\pi} \cdot \kappa_s \cdot \omega_o \cdot \sqrt{1 + r^2}}}{T_{sub} - T_k}\right]\right\}. \tag{3.19}$$

A simple fixed-point iteration method can be implemented to numerically solve such an equation. Figure 3.2 is a plot of the temperature distributing calculated from (3.19) for a polystyrene film on silicon for various incident laser powers.

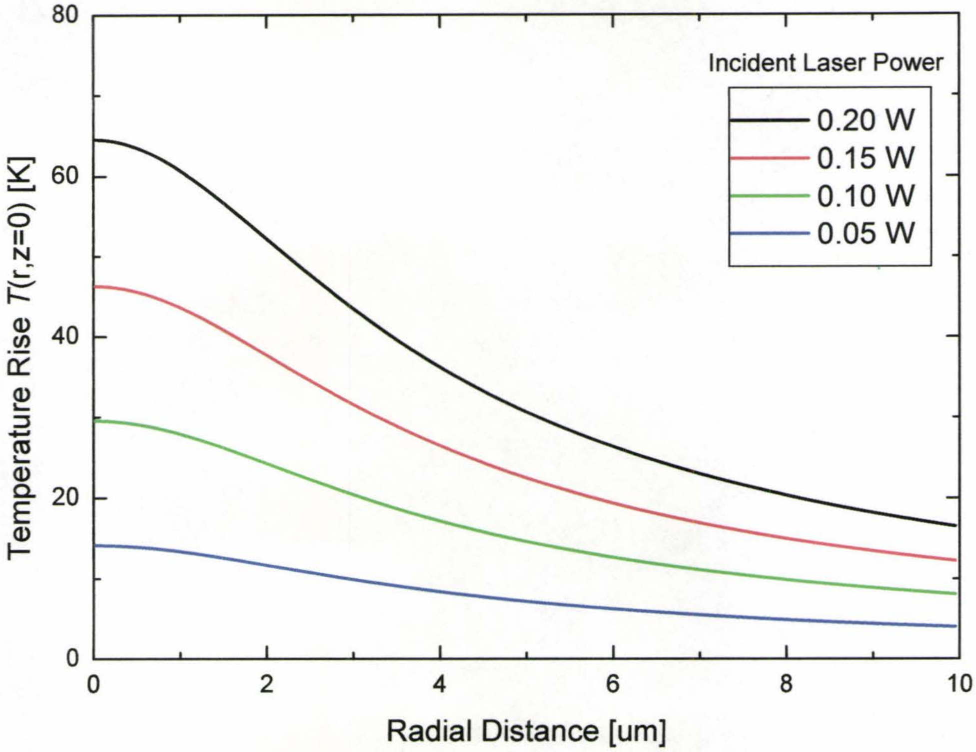

Figure 3.2: Calculated temperature distribution, see eq. (3.19), of an incident 532 nm *cw* laser focused ($\omega_o = 3.02$ μm) onto bare silicon taking into account the temperature dependent nature of α_s and κ_s and R. Where $R(\lambda,T_o) = 0.3734$, $T_o = 298$ K and $\eta = 0$.

As expected, the temperature rise is highest at the center of the incident beam ($r = 0$) and smoothly decreases radially outward away from the irradiation zone. Increasing laser power is seen to raise the central temperature rise and sharpen the spatial distribution. As discussed in Section 1.2.4, it is not the absolute temperature rise that is important, but rather the thermal *gradient* that drives the lithography process. Figure 3.3 is a calculated plot of some achievable thermal gradients, shown to exceed 1,500,000 °C/cm for very modest laser powers. The gradients were determined from the profiles of equation (3.19) calculated as the temperature drop from 0 to 4 μm.

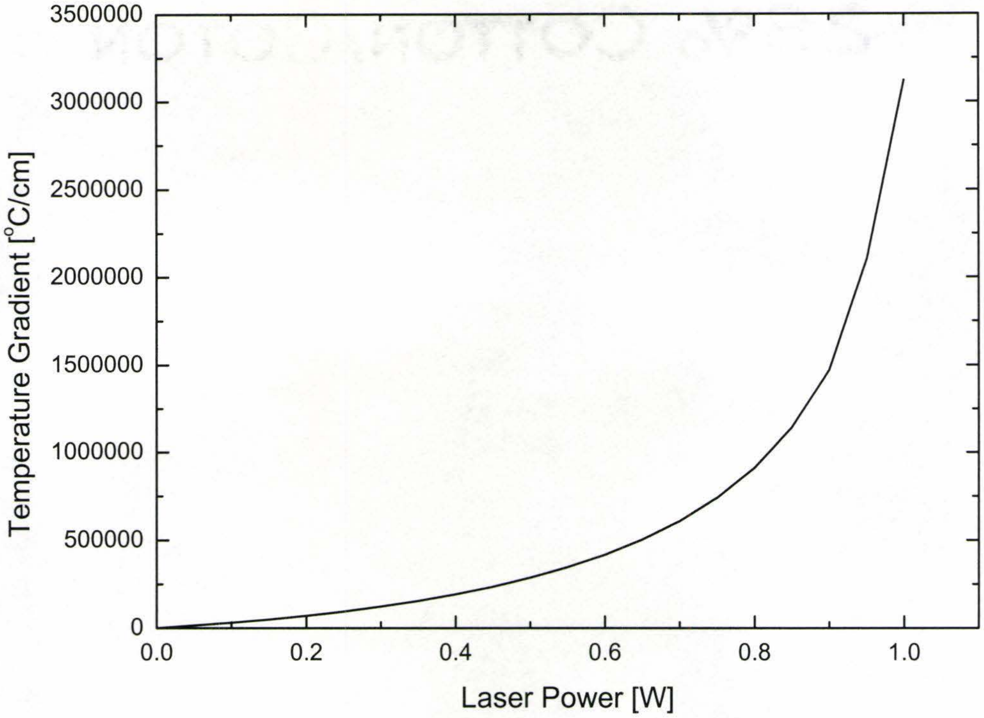

Figure 3.3: Temperature gradients calculated from Figure 3.2 and equation (3.19).

3.5 Thin Film Interference Effects on the Temperature Rise

The influence of the thin polymer film coating the substrate has been ignored up to this point in the thermal modelling of the previous sections. It will now be shown that effects of the film should not be ignored for a full understanding of the behaviour of the lithography system. Following a mathematical treatment of the problem, experimental evidence proving the significance of the effect will be revealed and discussed.

3.5.1 Reflectivity and the Fresnel Equations

Silicon, the substrate material for all of the samples discussed in this thesis, has a refractive index of 4.142 at 532 nm and absorbs 63% of the laser light incident upon its surface. The remaining power (37%), is reflected back into the medium through which it came. These power fractions are described by the *reflectance* (*R*) and *transmittance* (*T*), which depend on the ratio of the squares of the electric field amplitudes, determined by the Fresnel equations [18]:

$$\begin{aligned} r_{TE} &= \frac{E_r}{E_o} = \frac{\cos\theta - \sqrt{n^2 - \sin^2\theta}}{\cos\theta + \sqrt{n^2 - \sin^2\theta}} & r_{TM} &= \frac{E_r}{E_o} = \frac{n^2\cos\theta - \sqrt{n^2 - \sin^2\theta}}{n^2\cos\theta + \sqrt{n^2 - \sin^2\theta}} \\ t_{TE} &= \frac{E_t}{E_o} = \frac{2\cos\theta}{\cos\theta + \sqrt{n^2 - \sin^2\theta}} & t_{TM} &= \frac{E_t}{E_o} = \frac{2n\cos\theta}{n^2\cos\theta + \sqrt{n^2 - \sin^2\theta}} \end{aligned} \quad ; \quad (3.20)$$

where r and t are the reflection and transmission coefficients. TM and TE distinguish between the transverse magnetic and transverse electric orientations. E_r, E_t and E_o are the reflected, transmitted and initial electric field intensities. θ is the angle of incidence and n the relative refractive index, defined as $n = n_S/n_M$.

For the case of normal incidence, (R) and (T) are given by:

$$R = r^2 = \left(\frac{1-n}{1+n}\right)^2 \text{ and } T = t^2 = 1 - R. \qquad (3.21)$$

The significance of the reflectance coefficient becomes clear when calculating the laser induced temperature rise outlined in the previous section. The fraction of power (P) that is responsible for the temperature rise, compared to the total incident power (P_o), is simply $P = P_o(1 - R)$. Unfortunately, R cannot be calculated by considering the optical properties of the substrate alone, as additional allowances must be made to include the optical interference effects of the polymer film coating.

3.5.2 Reflectance of a Thin Film

Theoretical treatment of thin film reflectors is typically done by setting up a mathematical transfer matrix that accounts for the incurred phase differences and material properties of the thin film system [17].

$$\begin{bmatrix} E_a \\ B_a \end{bmatrix} = \begin{bmatrix} \cos\delta & \dfrac{i\sin\delta}{n_j\sqrt{\varepsilon_o\mu_o}\cos\theta_j} \\ in_1\sqrt{\varepsilon_o\mu_o}\cos\theta_1 & \cos\delta \end{bmatrix} \begin{bmatrix} E_b \\ B_b \end{bmatrix}; \qquad (3.22)$$

where $E_{a,b}$ and $B_{a,b}$ are the electric and magnetic field amplitudes in the mediums a & b, μ_o and ϵ_o are the permeability and permittivity of free space and n_j and θ_j the refractive index and angle of incidence in the medium j. δ is the phase difference accumulated by a wave of wavelength λ_o over the transversal of one film thickness h, otherwise defined as:

$$\delta = \left(\frac{2\pi}{\lambda_o}\right)\cdot n_j \cdot t \cdot \cos\left(\theta_j\right). \tag{3.23}$$

The advantage of the matrix treatment of the problem is that it is easily extended to systems consisting of more than one layer. Where the generalized form for a multi-layer system of N arbitrary layers is simply [17]:

$$\begin{bmatrix} E_a \\ B_a \end{bmatrix} = M_1 M_2 \cdots M_N \begin{bmatrix} E_N \\ B_N \end{bmatrix}. \tag{3.24}$$

For the current 1-layer system, at normal incidence, the reflection coefficient is determined by [18]:

$$r = \frac{E_{r1}}{E_o} = \frac{n_1\left(n_o - n_s\right)\cos\delta + i\left(n_o n_s - n_1^2\right)\sin\delta}{n_1\left(n_o + n_s\right)\cos\delta + i\left(n_o n_s + n_1^2\right)\sin\delta}. \tag{3.25}$$

The reflectance R for a one-layer thin film system is calculated for normal incidence by:

$$R = r^2 = \frac{n_1^2\left(n_o - n_s\right)^2 \cos\delta + \left(n_o n_s - n_1^2\right)^2 \sin^2\delta}{n_1^2\left(n_o + n_s\right)^2 \cos\delta + \left(n_o n_s + n_1^2\right)^2 \sin^2\delta}. \tag{3.26}$$

For a smooth layer of polystyrene coating a silicon substrate, the reflectance as a function of film thickness is calculated using equation (3.26) and is plotted in Figure 34.

Figure 3.4 demonstrates that a linear variation in the film thickness results in a oscillatory shift in the reflectance with a period of λ/2 and maximum reflectance change on the order of 30%. This implies that films of differing initial thickness will be subjected to differing induced temperature distributions for the same incident laser power. This effect can be quantified by returning to the temperature model of section 3.4. The reflectance for various film thicknesses was calculated and substituted into equation (3.19) in order to estimate the maximum temperature rise of a 0.20 W beam on a polystyrene coated silicon substrate. The results are plotted in Figure 3.5.

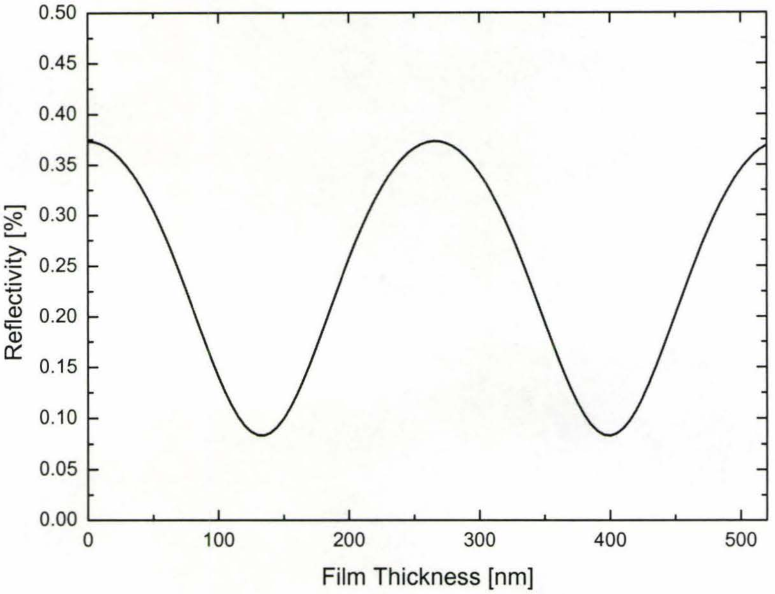

Figure 3.4: Reflectance as a function of film thickness for a thin film of PS (n = 1.512) on Si ($n = 4.142$).

From Figure 3.5, we see that the temperature oscillates between ~64 °C and ~103 °C with a peak-to-peak variance of ~39 °C. This variation becomes even more substantial for higher laser powers.

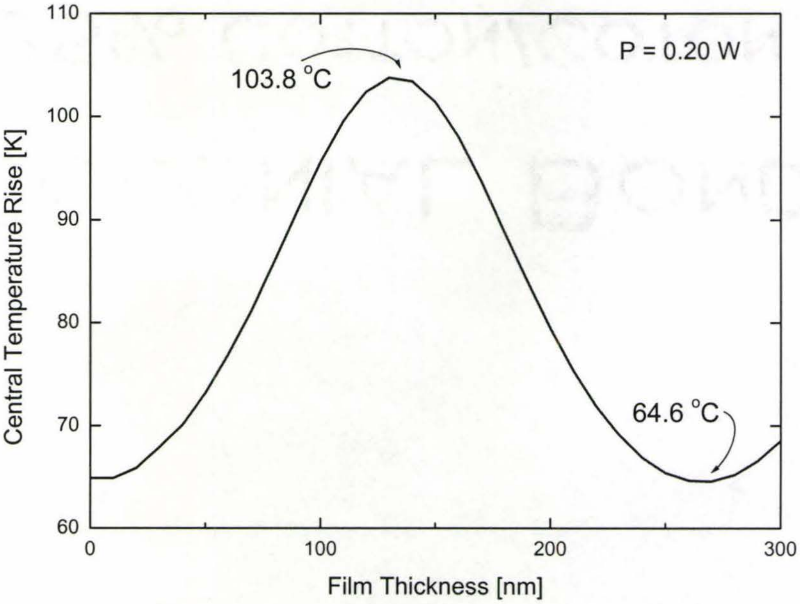

Figure 3.5: Calculated temperature rise (3.19) vs. the thickness of a polystyrene film on silicon. Incident laser power = 0.20 W. κ(Si) =150 W/mK, λ = 532 nm, $\alpha = 5.0 \times 10^3$ cm^{-1}, $\omega_o = 3.02$ μm, $T_{sub} = 298$ K.

3.6 Temperature Calibration: Experimental Verification

To verify the model used to describe the temperature profile including interference effects we employ a simple calibration procedure. This same procedure is used to verify the accuracy of the Feedback Mode control loop, introduced in Section 2.2.5, in producing a constant absorbed power. The following section will describe the temperature calibration procedure, discus its validity and explain any sources of discrepancy.

3.6.1 Experimental Procedure

A thin film of poly(ethylene oxide) was chosen as a calibrating material because it has a very sharp crystallization temperature (62 ± 1 ^{o}C, as measured with a Linkam THMS 600 heating stage). A thin film of PEO was spincast onto a clean, bare silicon substrate. A series of lines were then imprinted onto the film by slowly scanning (0.001 mm/s) a focused laser beam across its surface. Running the laser in Feedback Mode, the absorbed laser power was incrementally decreased with each subsequent pass. The film was then visually inspected with optical microscopy. When the laser power becomes insufficient to melt the film, a condition denoted by the absence of any laser markings, we can assume that the laser induced temperature at the last visible line is equivalent to the melting temperature of PEO. Repeating the experiment for different film thickness while running the laser in FM also serves as a proof of the effectiveness of the feedback laser routine.

3.6.2 Results

Figure 3.6 presents two optical microscope images of a series of decreasing power laser lines drawn into two separate PEO films of differing initial thickness. We see that, as the laser power is decreased, the marker lines (indicating a melted film) become increasingly faint until ultimately disappearing. It is seen that both patterns contain the same number of lines, the last of which was created with an absorbed power (in Feedback Mode) of 0.065 W, indicating that the threshold laser power for surface melting of each film is the identical.

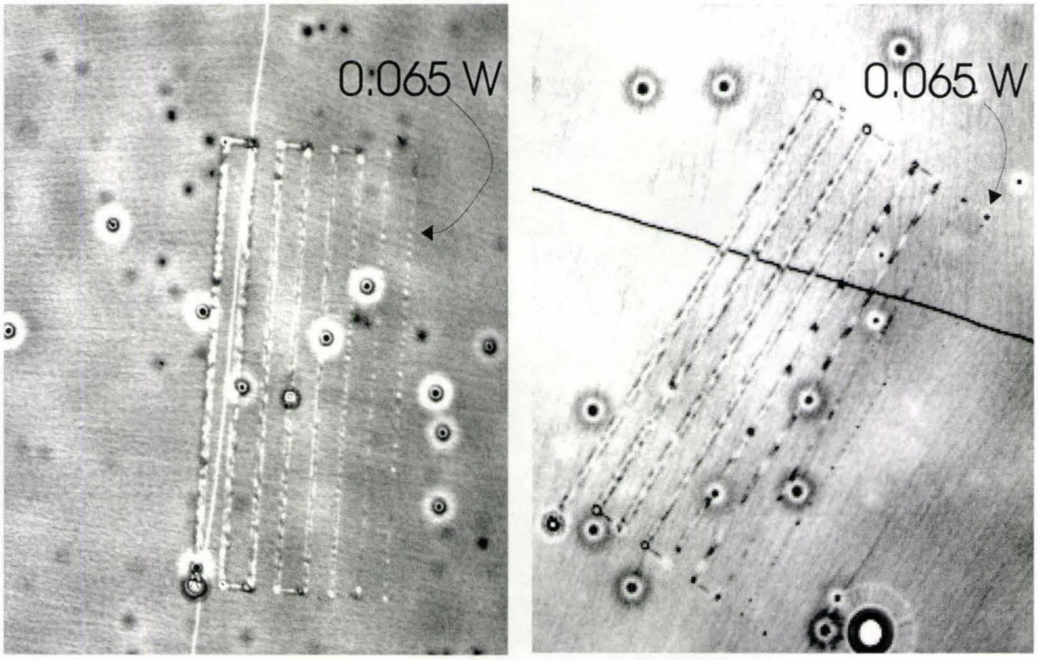

Figure 3.6: Optical microscope images of laser trenches drawn into two films of PEO of different initial thickness. The faintest mark was made by a laser power of 0.065 W. h = 420 nm and 395 nm. Scale (0.5 x 0.4 mm).

From the above figure, we can conclude that P = 0.065 W corresponds to a temperature rise equivalent to the melting temperature of the film. Returning to equation (3.19), the maximum expected temperature rise at $r = 0$ is calculated as 31.62 K above an initial substrate temperature of 298 K. In comparing the calculated temperature (~59 °C) with the experimental (~62 °C), we can conclude that equation (3.19) provides a reasonably good estimate of the projected temperature rise induced by a focused laser.

Chapter 4

Observed Patterns and Behaviours

A substantial portion of the efforts described in this thesis was devoted to the initial construction and design of the lithography apparatus, computer interfacing of the components and above all, exploring the behaviour of thin polymer films in the presence of localized thermal gradients. Presented in this chapter are the various experiments and resultant behaviours observed during the patterning of thin polymer films with a focused laser beam. The first few sections of this chapter will explore the working mechanism of the lithography process and provide an intuitive understanding for the significance of time, incident power and film thickness on the observed behaviour. Subsequent sections will provide a short review of high power effects as well as introduce lithographic patterning of other material systems. The chapter concludes with a brief examination of applications.

4.1 The Working Mechanism of Laser Lithography

Shown in Figure 4.1 are two typical AFM images that illustrate the characteristic response of a thin polymer film to both a translating (a) and stationary (b) focused *cw* laser beam. The patterns seen in (a) were formed by scanning the laser across the surface of the sample at a constant speed for different laser powers. Qualitatively, we see that increasing the laser power results in a more pronounced effect, creating deeper and wider indentations. Figure 4.1 (b) is a picture of a deformation created by holding the laser beam in a fixed position on the surface of a polymer film. While both of these structures were formed in different ways, qualitatively they share similar features—The presence of the focused laser beam is seen to push the polymer film away from the center of the beam focus. The removed material is deposited on a smooth and continous ridge perpendicular to the direction of the beam propagation (Fig. 4.1 (a)) or on a rim around the perimeter of the deformation (Fig. 4.1 (b)). The observation of the rim prompted a closer investigation of the surface profiles.

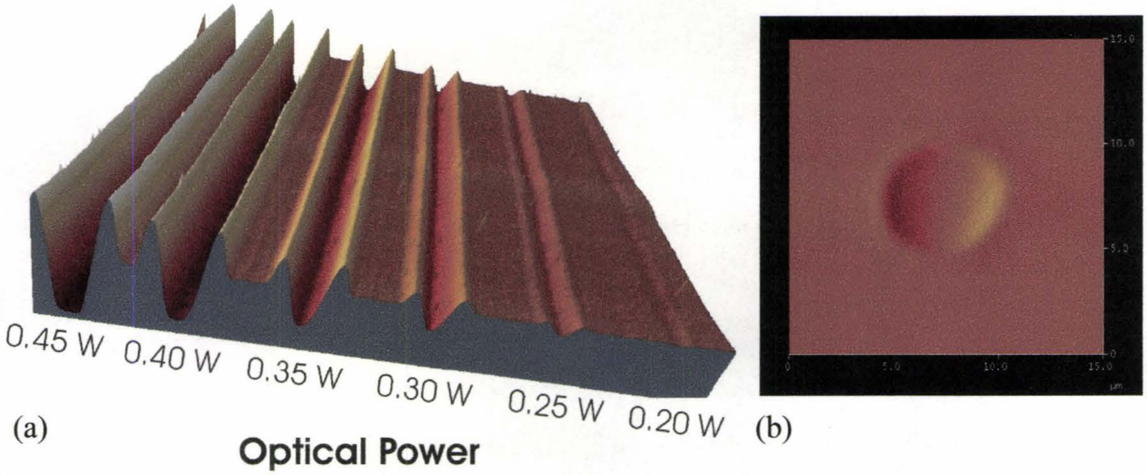

Figure 4.1: Sample atomic force microscopy images of two laser formed structures in a thin film of polystyrene on silicon. (a) is an amplitude image of a series of laser trenches cut at a constant velocity for increasing focused powers, scale (x/y = 50 μm, z = 250 nm) (b) is an error plot, which can be thought of as the AFM height derivative, of the initial stages of a laser dimple or hole. Scale (x/y = 15 μm).

A cross section of a deformation similar to that shown in Figure 4.1 (b) was measured with atomic force microscopy and is plotted in Figure 4.2. After scaling the horizontal axis by a factor of $2\pi r$ to accommodate for the circular shape of the hole, the depth data was numerically integrated in order to determine the fraction of material above and below the initial height of the film. The results of the calculation on the profile of Figure 4.2 and others reveal that the volume of the film is conserved—Indicating that the driving mechanism of the lithography process is of a non-destructive nature. With this observation in mind, two possible mechanisms that could produce such a deformation, without the loss of material, were proposed.

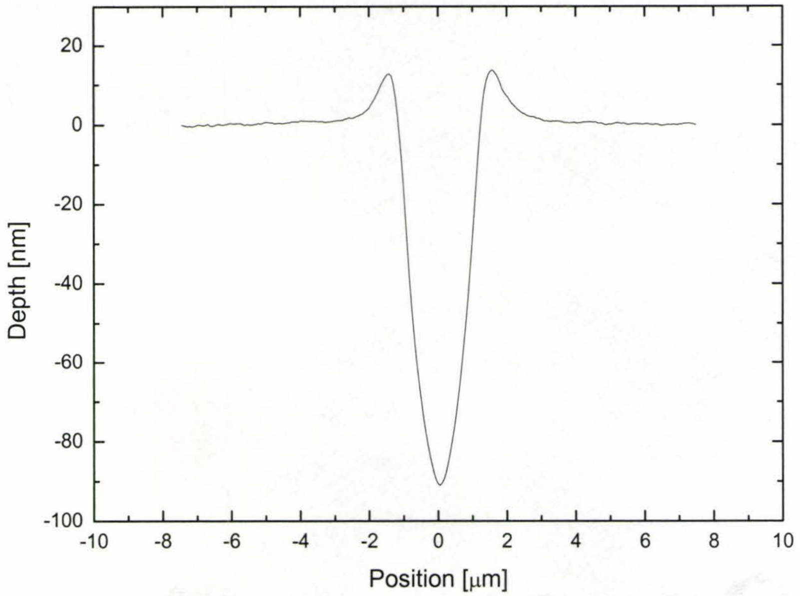

Figure 4.2: Typical cross sectional profile of a dimple formed by a focused laser beam. Film: Polystyrene on silicon, initial thickness 232 nm, irradiation time 260 s and incident laser power 0.04 W. The sample was initially heated to T_{sub} = 110 °C

4.1.1 Photonic Forces

It has long been known that light possesses an inherent momentum[1]. As with any collision, the laws of conservation of energy and momentum equally govern the interactions that occur between light and matter. Thus, when light strikes the surface of a material, a small force, or recoil pressure, is generated following refraction, reflection and absorption. Although the magnitude of the force of an individual photon is small (on the order of pico Newtons), the advent of high intensity light sources has enabled scientists to exploit these small forces to grasp onto and manipulates particles [28], cool atoms to extreme temperatures [29], distort cellular membranes [30] and even deform liquid surfaces [31]. With these studies in mind, it was initially proposed that a small radiation pressure, applied to the surface of a polymer melt, could be the source of the characteristic profiles observed in Figures 4.1 and 4.2. However, a calculation, performed in Appendix A, determines that for the thin film systems described in this thesis, the

---

[1] The momentum p of a photon with wavelength λ is determined by $p = h / \lambda$. Where h is Planck's constant: 6.626 x 10^{-34}J s. [32]

resultant force is both small in magnitude and, more importantly, directed in the opposite direction required to form the observed indentations.

4.1.2 The Marangoni or Thermocapillary Effect

The second proposed mechanism, as described in the introductory chapter, is the Marangoni or thermocapillary effect. In the presence of a thermal gradient, a force imbalance is generated on the surface of a liquid due to the temperature dependent nature of the surface tension. This asymmetry leads to a flow of material from the area of low surface tension to that of high surface tension.

Having estimated the temperature gradients that can be generated by a focused laser beam in Chapter 3, we can roughly quantify the thermocapillary effect:

Estimating the temperature gradient for $P = 0.20$ W from Figure 3.2 as:

$$\frac{\partial T}{\partial r} = \frac{57\ K}{4\ \mu m} = -14,250,000\ \frac{\mathrm{K}}{\mathrm{m}}. \tag{4.1}$$

The temperature dependence of the surface tension of polystyrene (see section 1.2.3) is:

$$\frac{\partial \gamma}{\partial T} = -0.072\ \frac{\mathrm{dyne}}{\mathrm{cm}\cdot\mathrm{K}}. \tag{4.2}$$

The resultant surface pressure $\nabla\gamma$ is then:

$$\nabla\gamma = \frac{\partial T}{\partial r}\cdot\frac{\partial \gamma}{\partial T} = 1026\ \frac{\mathrm{N}}{\mathrm{m}} \tag{4.3}$$

For a film thickness h of 500 nm and estimated viscosity $\eta \sim 10^3$ Poise, the surface velocity v of such a system is calculated to be (see eq. (1.1)):

$$v = \frac{\nabla\gamma}{\eta}\cdot h \approx 0.51\ \frac{\mu\mathrm{m}}{\mathrm{s}} \tag{4.4}$$

While a surface velocity on the order of microns/second seems numerically small, it remains large enough to be observable within experimental time scales and dimensions. Clearly, the thermocapillary force is significant enough to account for the laser lithography process.

4.2 Characterization of the Marangoni Effect

One of the most important descriptions of any system or effect is how it evolves with time. Fortunately, the temporal and other parameter dependent behaviours of the laser driven Marangoni effect in thin polymer films can be examined with a few simple experiments.

4.2.1 Temporal Evolution of the Marangoni Effect

By irradiating a thin film for varying amounts of time and measuring each of the surface profiles by AFM, a time sequence, representing a complete hole evolution can be compiled for different laser powers and initial film thicknesses. For the experiments described in this section, all samples are composed of thin polystyrene films (225 nm – 244 nm) on silicon substrates. Prior to irradiation, the temperature of each sample is raised to 110 °C by the heating stage of the sample mount. With the glass transition temperature of PS being ~100 °C, this ensures that the polymer film is in its melt state and is able to flow. Otherwise, the focused laser would be responsible for both the Marangoni effect *and* melting—which complicates the analysis.

Figure 4.3 is an optical microscope image of a typical experiment, where a separate region of the film is irradiated in sequence for an increasing period of time. The top row of holes was formed at a high power and fixed irradiation time and is present simply to assist locating the experimental region.

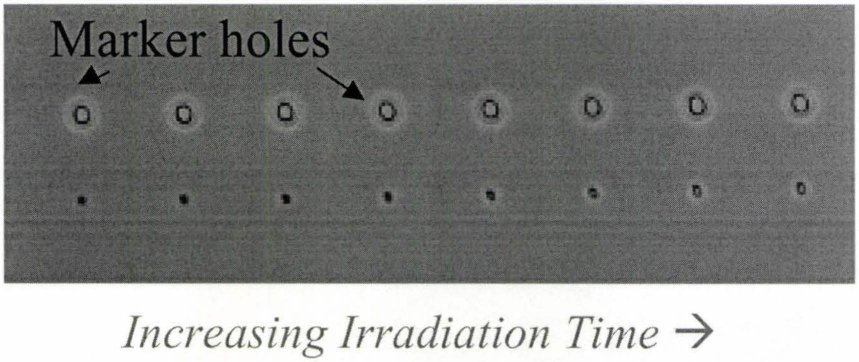

Figure 4.3: Optical microscopy image, scale (200 μm x 50 μm), of a sequence of laser heated deformations in a 275 nm PS film on a silicon substrate. Irradiation times were varied from 165 s to 795 s in increments of 90 s with an incident power of 0.12 W. The entire sample was raised to 110 °C prior to irradiation.

Generating a time sequence in this fashion was the source of some initial concern regarding the stability of the surface profiles over the total time of the experiment. Since the polymer film is held above its glass transition temperature (and is therefore liquid like and deformable), it is possible that a dimple created at the beginning of the experiment would relax and flatten while its neighbours were being formed. It was however experimentally verified that very little relaxation (on the order of statistical variance) occurs over the time period of experiments under 90 minutes in total length. Once the sequence is complete, the entire sample is removed from the heating stage and quenched on a cool piece of metal, permanently freezing in the surface profiles that can then be quantified by optical and atomic force microscopy.

Figure 4.4 is a plot of the AFM cross sections of each hole in the time sequence of Figure 4.3. As expected, the longer the laser is held on a spot, the greater the observed effect. Although the cross sections represent different regions on the surface, the homogeneity of the sample and constancy of the experimental conditions allow us to imagine that the separate profiles represent the time evolution of a singular hole. From the figure, we see that the hole starts as a small indentation that slowly begins to deepen and widen with increasing irradiation time. As material flows away from the central region, it begins to pile up on a rim surrounding the perimeter, conserving volume throughout the process.

An interesting observation is seen between the final two profiles in the sequence. A sudden and dramatic increase in the maximum depth is observed between the longest two irradiation times. Repeated trials produced similar results, indicating that this is a characteristic behaviour of the system. It will be shown in Section 4.2.4 that this can be understood based on the interference effects of the thin film coating.

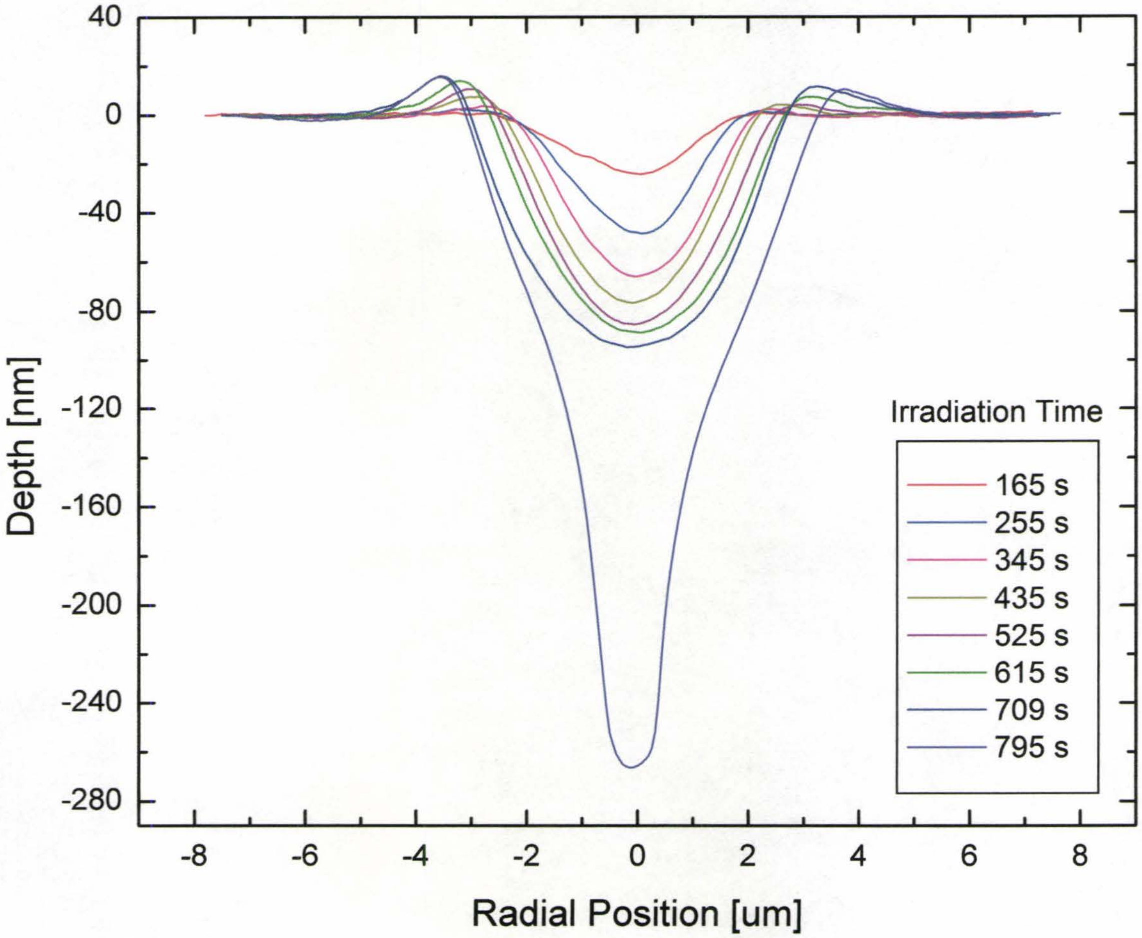

Figure 4.4: Sequential cross sectional depth profiles of Marangoni driven surface deformations, as measured by atomic force microscopy. PS film on silicon with an initial film thickness of 275 nm. Irradiation times were between 165 and 795 s, incremented by 90 s with an incident laser power of 0.12 W. The sample was initially raised and held at T_{sub} = 110 °C.

4.2.2 Power Dependence

The temperature gradient that drives the thermocapillary effect is inherently linked to the laser power of the lithography system. With this in mind, a series of experiments, similar to the one described in the previous section, were repeated on different samples (nominally of the same thickness) with various incident laser powers in an effort to explore the power dependence of the Marangoni effect. From the AFM measurements of the surface profiles, the maximum depth of each cross section can be extracted and is plotted in Figure 4.5.

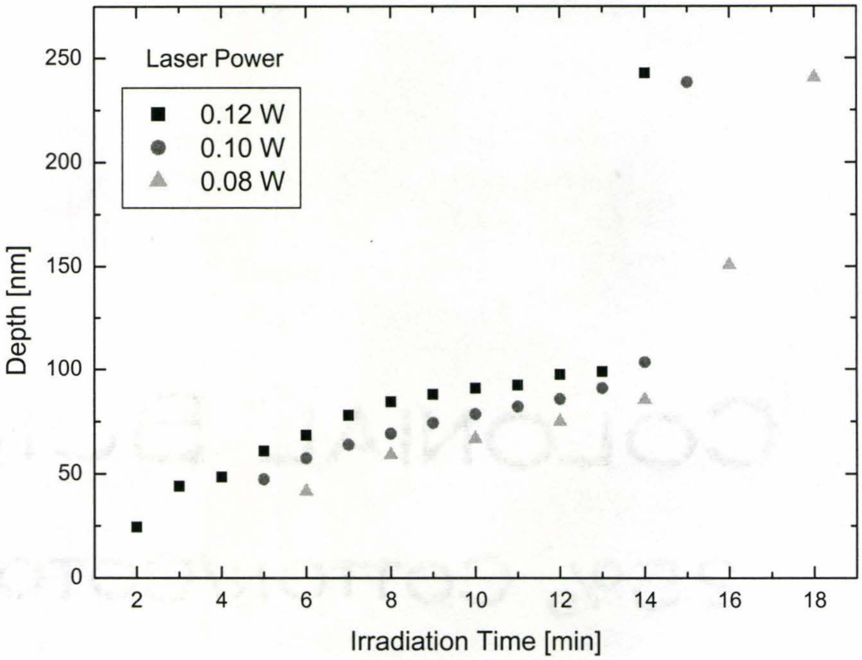

Figure 4.5: Maximum depth of a sequence of deformations in 244 nm PS films on silicon as measured by AFM. The samples were irradiated with incident laser powers of 0.12, 0.10 and 0.08 W for times between 0 and 18 minutes. T_{sub} = 110 °C.

It is seen from the above figure that each evolution has the same characteristic shape, as discussed in the previous section. After an initial steady increase in depth, the profiles are seen to level off before suddenly shooting to the substrate. It is observed from the lateral shift in the different plots that increasing the laser power simply accelerates the process, effectively decreasing the onset time before 'punch-through'. This power dependent behaviour can be easily understood by returning to our initial quantification of the thermocapillary effect discussed section 4.1.2 and specifically, by re-examining equation (4.4):

$$v = \frac{\nabla\gamma}{\eta} \cdot h \;\propto\; T \cdot \frac{h}{\eta} \;\propto\; P \cdot \frac{h}{\eta} \tag{4.5}$$

Qualitatively, equation (4.5) predicts the behaviour observed in Figure 4.5. The velocity of the material flow increases with the surface pressure $\nabla\gamma$, which is ultimately dependent upon the surface temperature rise or alternatively, the amount of laser power being absorbed into the substrate.

4.2.3 Dependence on Film Thickness

From equation (4.5), we would expect a velocity dependence on the film thickness *h*. Once again, this relationship can be verified by performing a similar experiment to the one described in the previous section. Maintaining the laser power constant between samples, the deformation profiles for three films of different initial thickness were measured by AFM. The maximum depth of each hole in the sequence is determined and the temporal evolution is plotted in Figure 4.6.

Figure 4.6 demonstrates the same characteristic trends observed in Figure 4.5, where

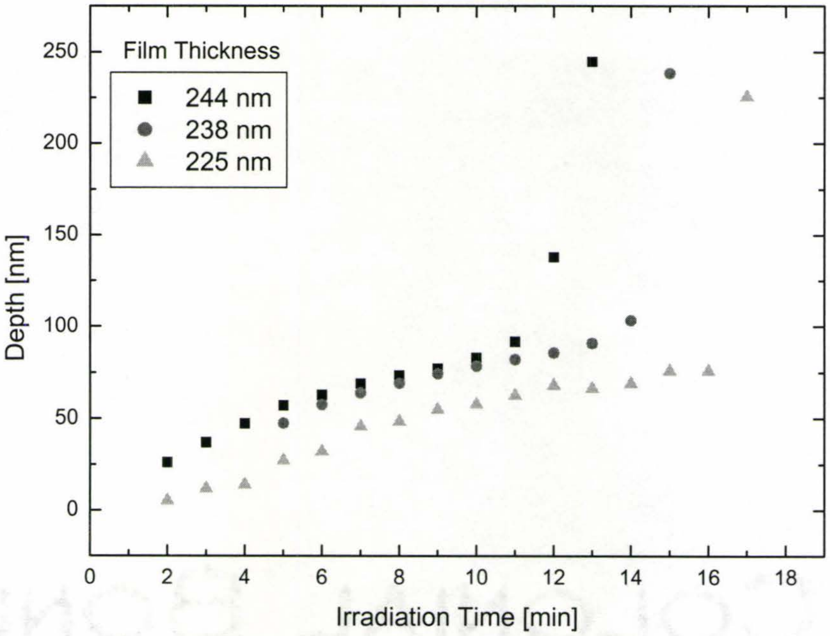

Figure 4.6: Maximum depth of a sequence of deformations in PS films on silicon with initial thickness *h* of 244, 238 and 225 nm, as measured by AFM. The samples were irradiated with an incident laser power of 0.10 W for times between 0 and 18 minutes. $T_{sub} = 110\ ^{\circ}C$.

the depths of the deformations go through a smooth evolution before rapidly punching through to the substrate.

4.2.4 Discussion of the Observed Behaviour

While the simple predictions of equation (4.5) shed some light onto the observed responses of Figures 4.5 and 4.6, the complex shape of the depth evolution is unexpected from a simple fluid dynamical treatment of the problem. Proper modelling of the lithography process will require additional physical considerations beyond the scope of this thesis. However, some immediate corrections can be suggested. Since the experiments are performed on thin films, the reliability of scaling macroscopic physics down to microscopic and nanoscopic length scales may be called to question, where the influence of the substrate-film interface and even the physical structure of the polymer melt may become important. The effects of additional polymer phenomenon such as shear thinning and the tremendous temperature dependence of the viscosity should be considered.

The data from Figures 4.5 and 4.6 is re-plotted as the remaining film thickness (at the maximum depth of the profile) as a function of time in Figure 4.7. An immediate trend is observed: The film thickness slowly decreases for each plot until it reaches a minimum value just under 150 nm before dramatically dropping to the substrate.

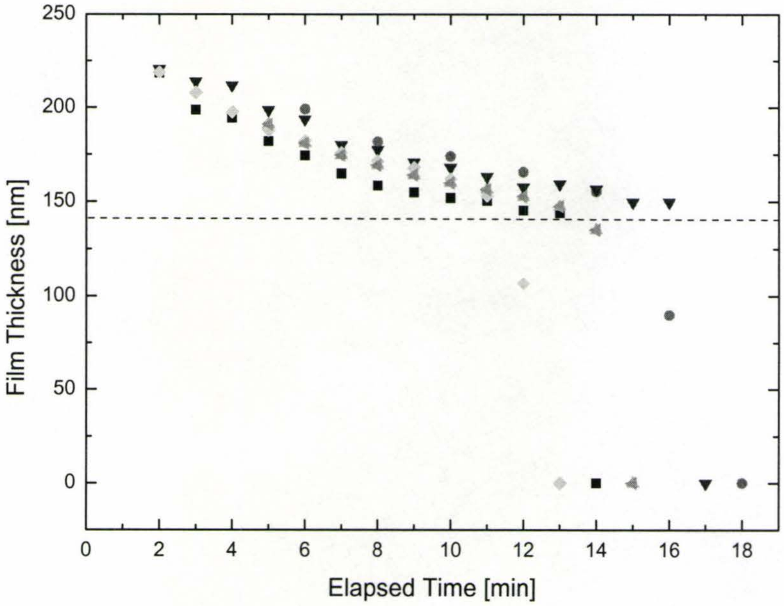

Figure 4.7: Remaining film thickness (at the location of maximal depth) as a function of time for the data previously shown in Figures 4.5 and 4.6.

This finding is not altogether surprising, since a minimum in the reflectance is expected for a thin film of polystyrene on silicon around this thickness (see Fig. 4.8). A reduction in the reflectance corresponds to an increase in the absorption by the sample and ultimately, an increase in the absorbed laser power and thermal gradient (Section 3.4.4). Thus, as the profile of the hole decreases the separation between the substrate and the surface of the film, local changes to the absorption properties of the sample and the induced temperature gradient occur *dynamically* with time.

Referring back to the observed behaviour of Figure 4.7 (i.e. "punch-through"), we can then propose that the sudden increase in the depth of the deformations is related to the increased temperature rise due to a change in the local reflectance of the film—leading to faster fluid flow.

Note: The experiments described to this point were all performed with a constant power incident onto the surface of the sample, before the development of the optical feedback control loop. In FM, the absorbed power is kept constant.

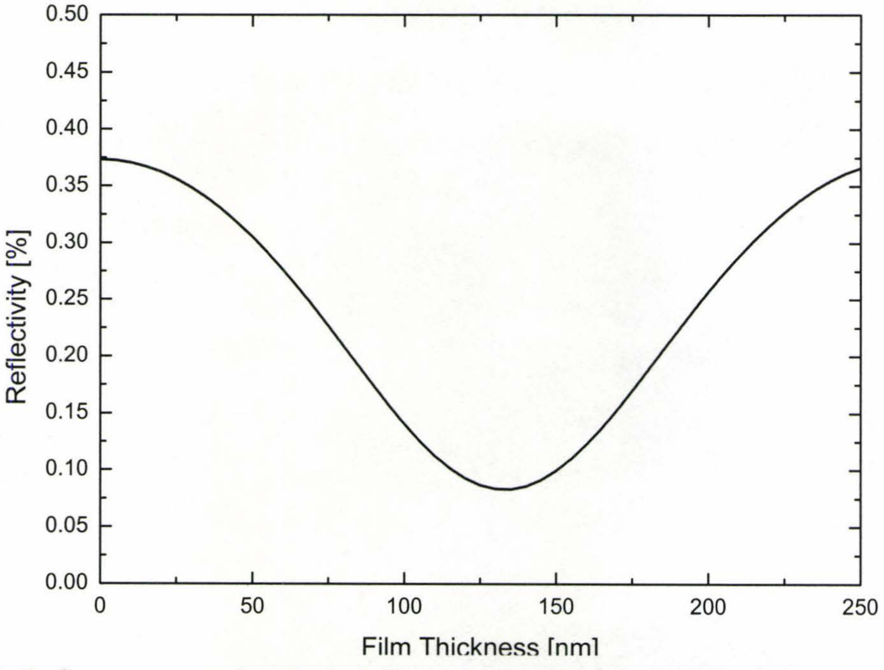

Figure 4.8: Reflectance as a function of film thickness for a polystyrene thin film on a silicon substrate.

4.2.5 Significance of the Interference Effect: Experimental Verification

The sensitivity of the film's absorption dependence on the nanoscopic features of the surface profiles can be verified with a straightforward experiment, presented in the following section. The principle behind the test is to locally measure the reflectance as a function of film thickness. This is accomplished by scanning a focused beam across a sample with a known variation in film thickness while monitoring the reflected power as a function of position. The first requirement was to manufacture an appropriate test sample. A gradient in film thickness was formed by laser patterning a series of varying depth trenches onto the surface of an initially flat sample (see Figure 4.9)

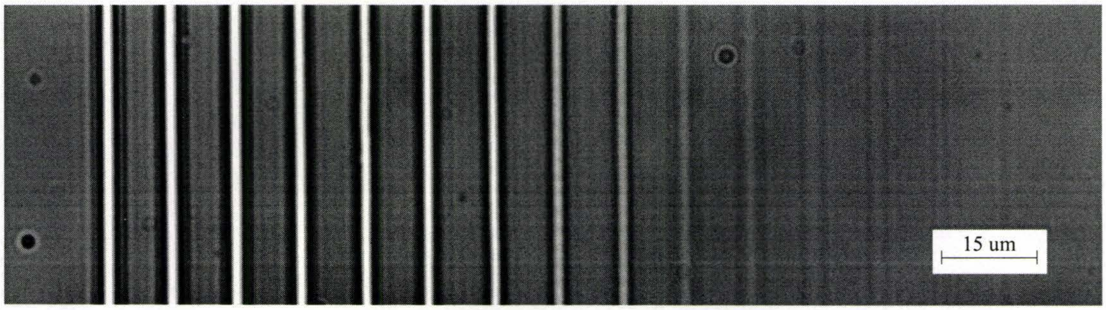

Figure 4.9: Varying depth laser trenches in a thin polystyrene film on silicon. Scale (135 x 45 μm).

While scanning the focused laser at low (0.04 W) incident power perpendicularly across the trenches, the reflected power was measured as a function of position in 0.1 μm increments. Plotting the results of the scan (Figure 4.10) reveals an intricate series of peaks, which follows the changes in the reflectance due to the variable surface profile.

A similar second scan was performed on a film with a different initial thickness. A closer inspection of its reflected power vs. position plot reveals the level of sensitivity of the effect (Fig. 4.11). We see that the measured reflected power is very responsive to the details of the laser trenches, providing a high resolution reflection map of the surface profile. In fact, one could imagine taking the values of the measured reflected power and converting them to a film thickness—potentially producing a high resolution film height vs. position surface profile.

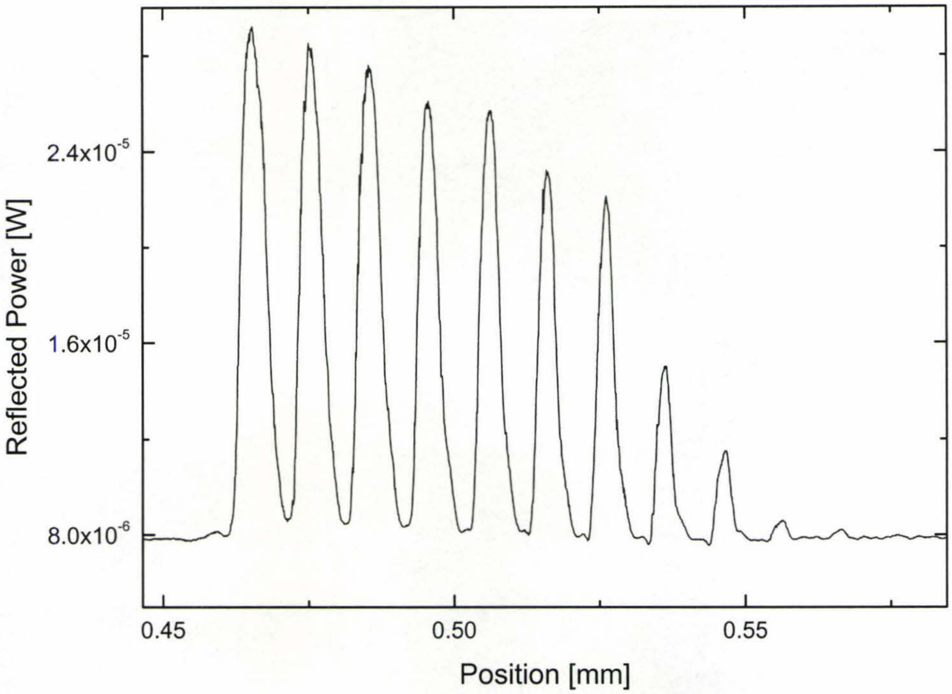

Figure 4.10: Measured reflected power vs. position of the pattern shown in Fig. 4.9. The height fluctuations across the sample are seen as changes in reflectance above the baseline of the initial film thickness.

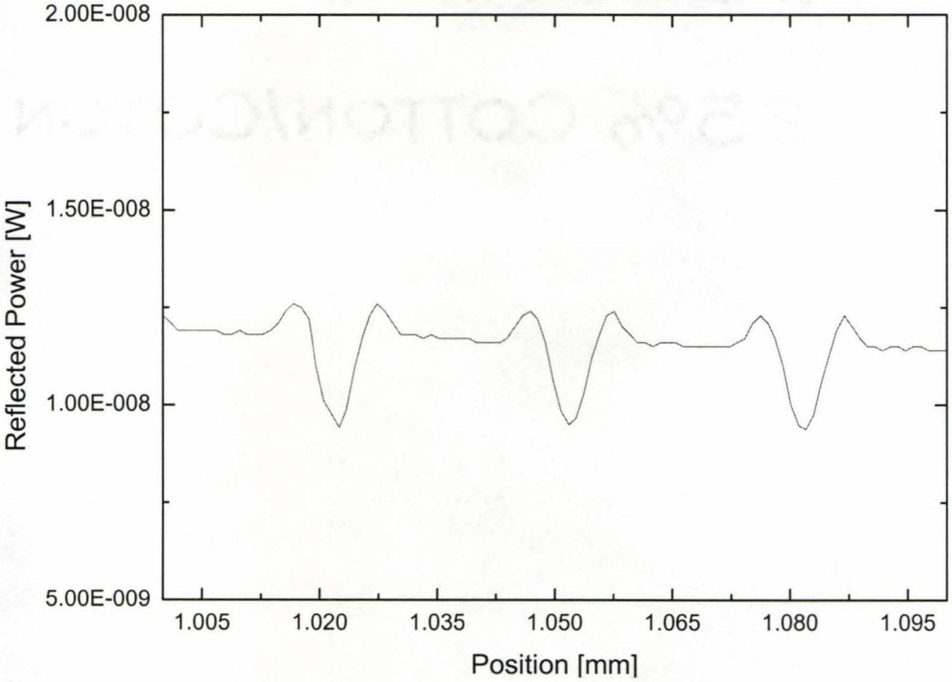

Figure 4.11: Closer inspection of a plot similar to the one displayed in Fig. 4.11. Reflected power as a function of position of the pattern shown in Figure 4.10. The plot closely follows the surface profile of the trenches.

4.3 Feedback Mode and Constant Absorbed Power

Figures 4.12 (a) and (b) represent the characteristic reflection behaviour over the course of an entire hole evolution (from an initially flat film to a bare substrate) for two different initial film thicknesses. Both curves demonstrate a complex progression as a result of the interference effects of the changing film profile. These plots offer further evidence of a dynamically varying temperature distribution. Plots such as these have motivated the development of a dynamic PID feedback control program that is designed to stabilize the induced temperature rise over the course of the irradiation time, discussed previously in Section 2.2.5.

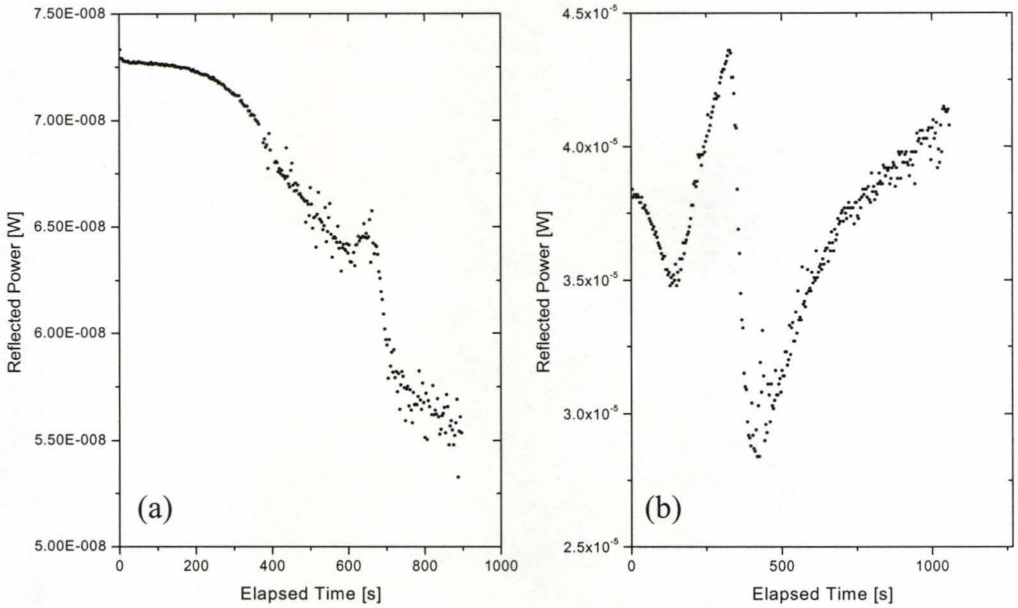

Figure 4.12: Measured reflected power as a function of time over the course of a hole evolution. (a) 300 nm film of PS on Si (b) 244 nm film of PS on Si. Absorbed laser power of 0.06 W. T_{sub} = 110 °C.

The governing principles behind the program are quite simple. As more power is reflected from the surface of a material, less energy is available to be absorbed and cause heating. We can account for this decrease in temperature by simply increasing the incident laser power by an amount equivalent to the energy lost by reflection. Conversely, when a decrease in the reflected power is observed, the laser power must be decreased to account of the increase in the absorption and heating. Thus, the laser power has to follow the rise and fall of the reflected power with time. Once the system is properly calibrated, the non-linear depth evolutions in Figure 4.7 could potentially be linearized, resulting in a more constant temperature distribution.

4.3.1 Temporal Evolution of the Marangoni Effect: Feedback Mode

Following a similar procedure detailed in Section 4.2.1, a sequence of evolving holes was created by irradiating a film, initially heated to 110 °C, for times between 2 and 8 minutes. The laser power, this time controlled by the feedback control routine, is set and maintained at a constant absorbed power of 0.04 W. When the series is complete, the sample is quenched on a cool piece of metal, freezing in the details of the evolution. The surface profiles of the individual holes are then measured by atomic force microscopy and the maximum depths extracted from the cross sections.

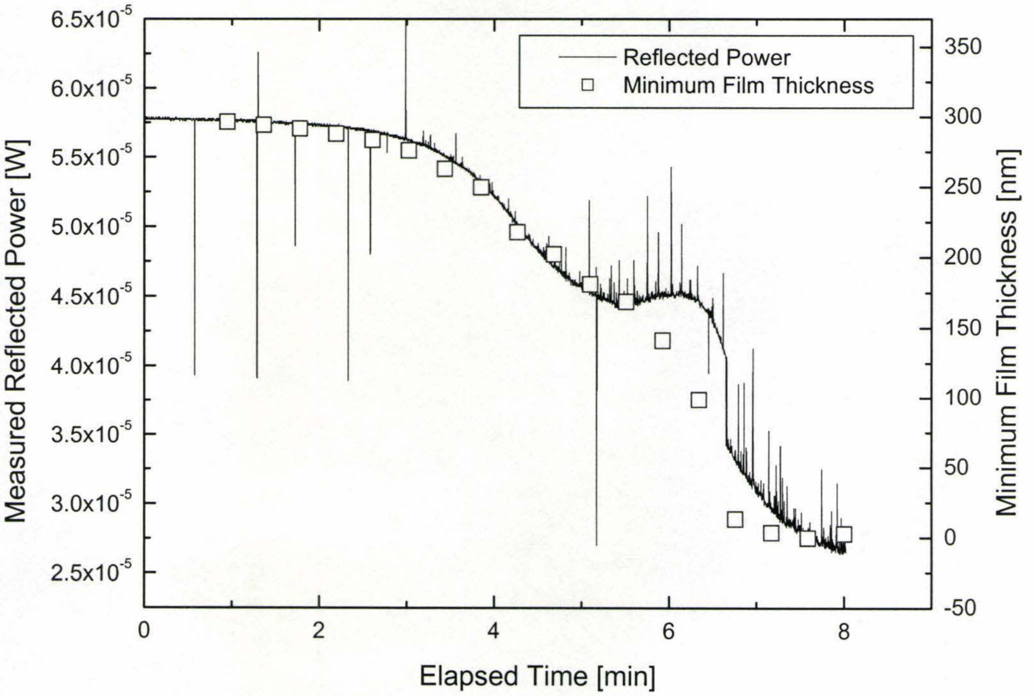

Figure 4.13 Comparison of the reflected power to the AFM measured minimum film thickness of a sequence of holes formed in a PS film on silicon. The laser was run in Feedback Mode with a constant absorbed power of 0.04 W. T_{sub} = 110 °C.

Figure 4.13 is a plot of the depth, as measured by AFM, of a sequence of holes and the corresponding change in the light detected by the power meter for the system running in Feedback Mode as a function of time. It is clear that, qualitatively, the two follow the same trend: An increase in the depth of the hole is marked by a decrease in the reflected power. This was predicted with the theoretical arguments of interference coatings.

A closer inspection of the AFM depth data reveals a much smoother evolution of the surface profiles compared to the previous runs (Figures 4.5 and 4.6) without the feedback control engaged. The sudden 'drop' in the film thickness to the substrate has been replaced by a more predictable, near exponential trend, as shown in Figure 4.14.

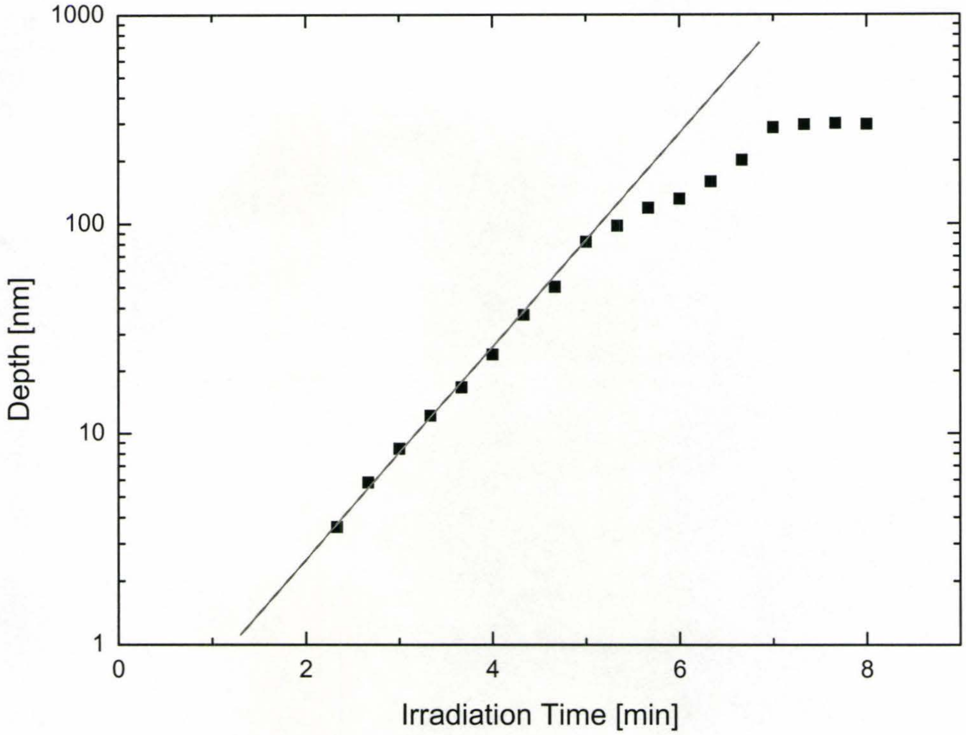

Figure 4.14: Maximum depth of a sequence of deformations in a PS film on silicon, semi-log plot. The laser is run in Feedback Mode with a constant absorbed power of 0.04 W. T_{sub} = 110 °C.

4.4 High Laser Power

The experiments described in the previous sections were performed at low laser power levels with experimental time scales extending from minutes to tens of minutes. It was observed that increasing the laser power had the effect of simply accelerating the formation of the pattern. Additionally, the experiments were executed by first raising the temperature of the sample with a heating stage to a level slightly above its glass transition temperature. This ensured that the entire polymer film behaved as a viscous fluid, avoiding the complications that may arise from a solid/liquid boundary in the experimental region.

The time evolution of dimples formed by high laser powers, with gradients exceeding 1,500,000 °C/cm, on room temperature films show some interesting characteristic differences from their low power counterparts. Figure 4.15 is a sample AFM image of a deformation created by a fast, high power laser shot onto a room temperature film of polystyrene on silicon. Immediately one notices the presence of *two* outer rims, which contrasts with the previous low power experiments where only one rim was observed. The temporal evolution of such a structure is presented sequentially in Figure 4.16. The first initial indent, formed within the first 0.02 seconds of the experiment, widens as a secondary rim begins to form in the center of the structure. This inner rim proceeds to evolve with the expected Marangoni profile. The final picture shows the usual indent profile with the addition of a small rim surrounding the elevated inner hole border.

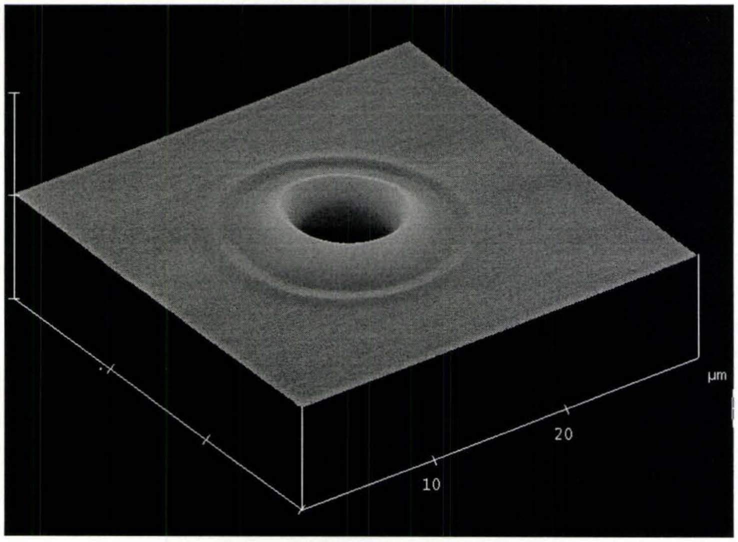

Figure 4.15: Atomic force micrograph of a incident 0.80 W, 0.16 s laser shot on a cold (T_{sub} = 25 °C) polystyrene film on silicon. Scale (x/y =10 μm, z = 800 nm).

While it was assumed that the non-destructive Marangoni effect was the sole mechanism driving the patterning, the extreme conditions presented by short, high power pulses could lead to additional phenomena. Regardless of the source of the double rim, the behaviour of a polymer film under the influence of extreme thermal gradients cannot be explained by the simple hydrodynamic treatment of the Marangoni effect discussed in this thesis.

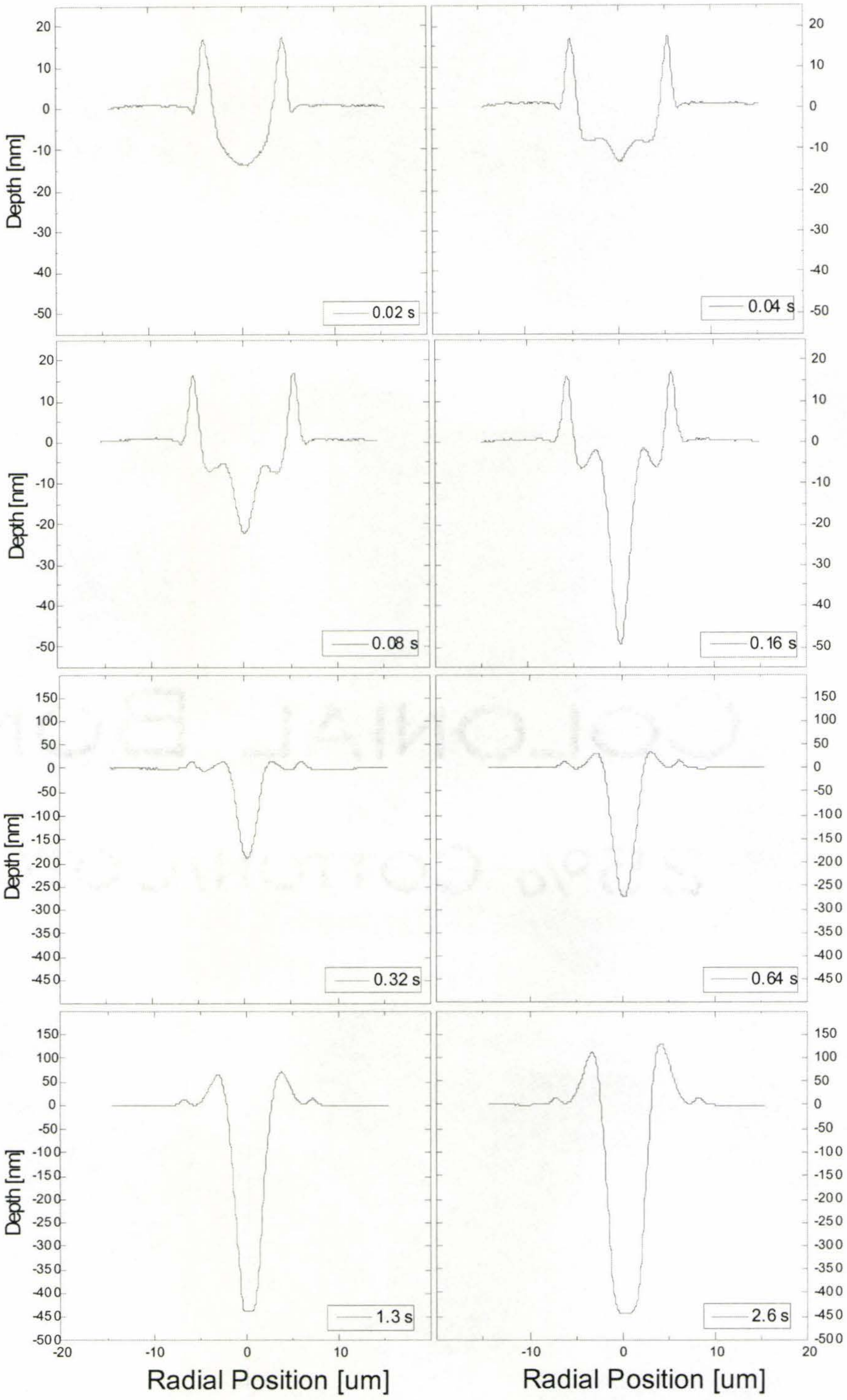

Figure 4.16: This sequence of cross sections demonstrates the time evolution of a 450 nm polystyrene film at $T_{sub} = 25\ ^{o}C$ subjected to an incident 0.80 W focused beam for irradiation times ranging from 0.02 to 2.6 s. The profiles were measured post-irradiation by atomic force microscopy. Note the change in the vertical scale from 0.16 s to 0.32 s.

4.5 Block Copolymer Phases

Marangoni driven laser lithography is not limited to a specific polymer thin film system and is extendable to any set of materials that can be melted and heated by laser radiation. Block co-polymers, which are macromolecules consisting of two or more chemically distinct tethered sub-chains, can also be patterned by this technique. They are an interesting subset of the polymer family due to their capability to spontaneously self-assemble into a variety of periodically ordered nano-structures [33-34]. A major draw for integrating these materials into the project is the potential merger of the micron-sized structures created by the lithography system with the inherent nanometre scale features of the block copolymers.

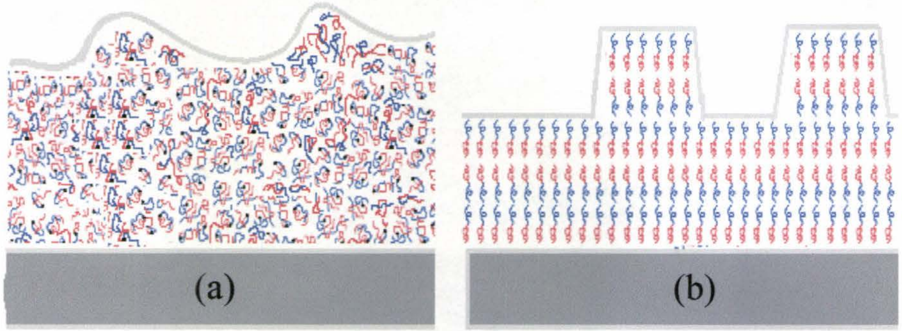

Figure 4.17: Schematical representation of a diblock film.
(a) Rippled (disordered) surface, (b) odered surface morphology

Figure 4.18 is an AFM image of a laser trench in a film of PS-b-PMMA that has been annealed below the order-to-disorder transition temperature (T_{ODT}) to form a sharp nano-structured surface (see Fig. 4.17). These AFM images clearly show the sharply defined nanoscopic (~20 nm step height) features of the block copolymer lamellar phases embedded into the microscopic profile of the laser trench.

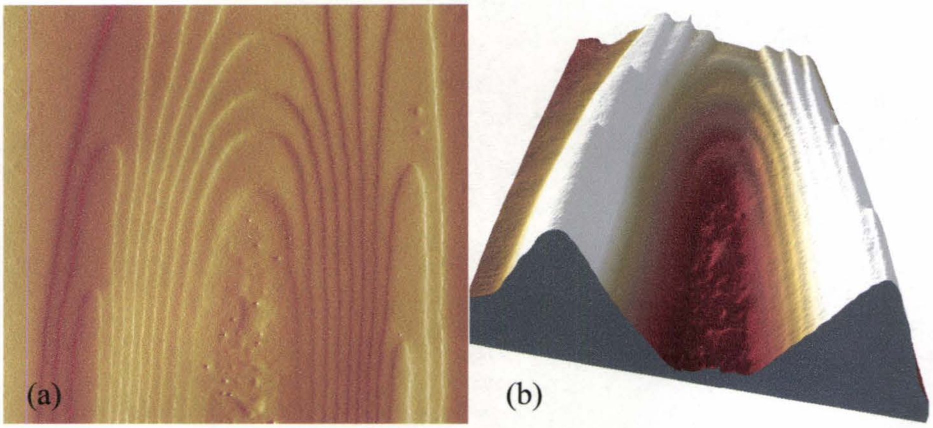

Figure 4.18: AFM image of an annealed PS-b-PMMA trench formed by laser lithography. The ridge structures shown in the picture are evidence of an ordered block copolymer lamellar phase. (a) Error signal, scale (x/y = 20 μm). (b) Height, scale (x/y = 20 μm, z = 200 nm).

Figure 4.19 is an series of images of a square grid cut into a film of PS-b-PMMA on silicon which was subsequently annealed on a heating stage below T_{ODT}. As the laser beam passes over the sample, it easily makes a trench through the film and exposes the bare substrate in the wake of its path. The non-destructive nature of the Marangoni effect simply takes this material and piles it onto the edges of the grid, creating an interesting, three-dimensional profile. Close inspection of the sidewalls of the structures with AFM reveal the nanometre features of the diblocks.

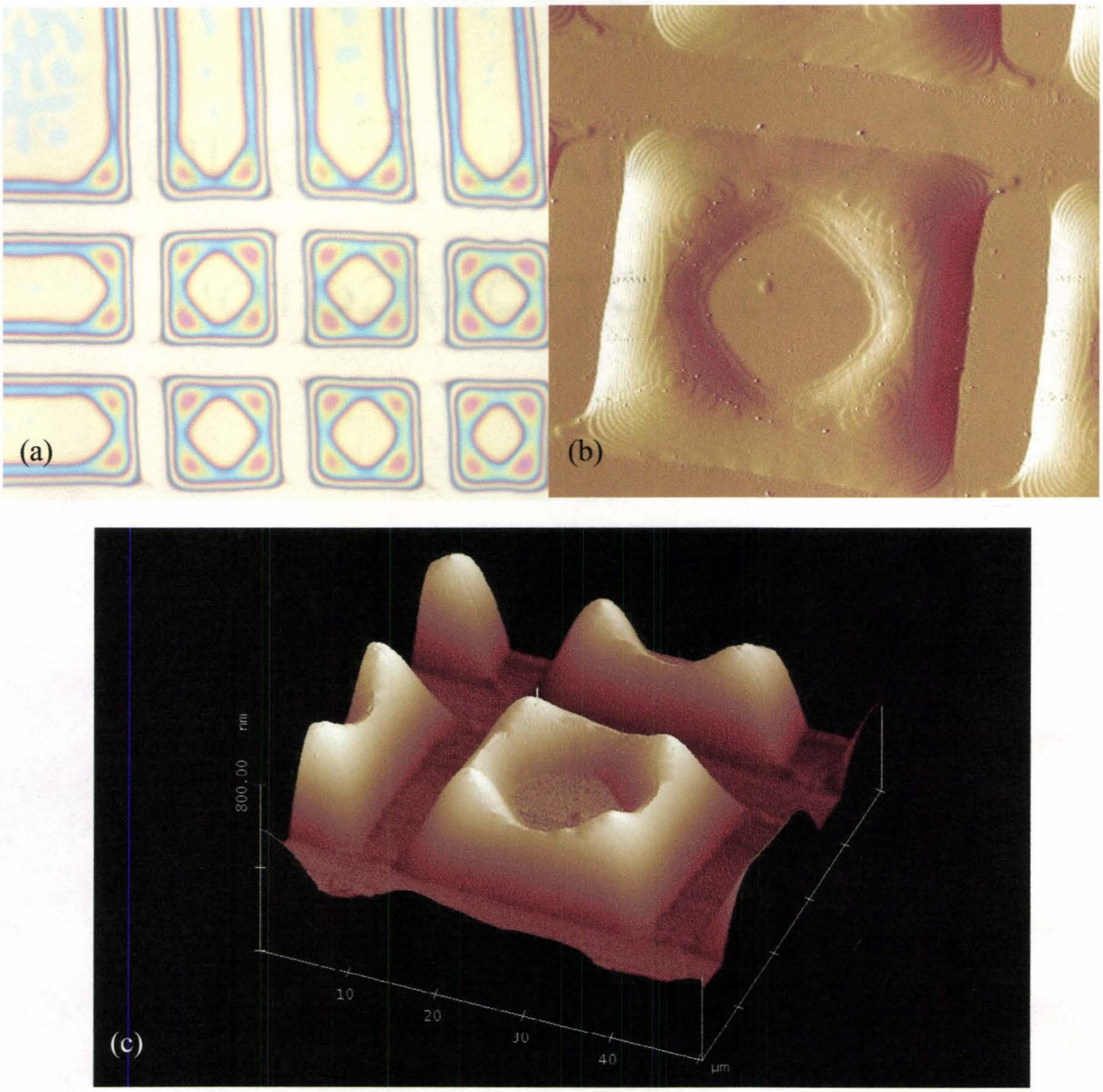

Figure 4.19: (a) Optical microscope image of a patterned PS-b-PMMA on Si film annealed at 130 °C for 60 minutes, scale (200 x 200 µm). (b) error signal (75 x 75 µm) & (c) height amplitude (x/y = 50 µm, z = 800 nm) AFM images of one of the squares structures pictured in (a).

4.6 Snow Plough Effect

When a focused beam is scanned back and forth across a sample with a small (~1 μm) incremental separation between each pass, the polymer film is swept or ploughed in the direction of the moving laser front, as shown in Figure 4.20.

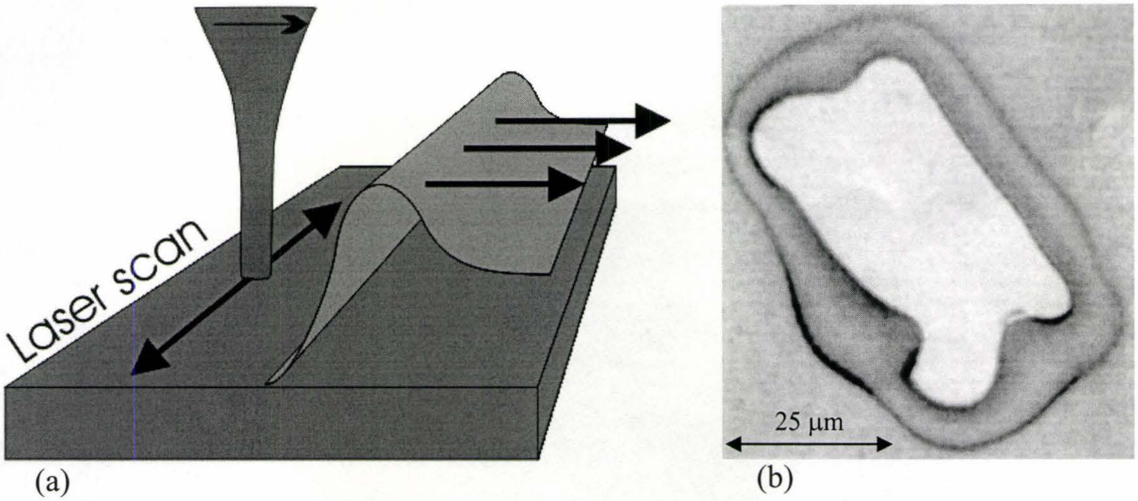

Figure 4.20: (a) Schematic of the plough effect. As the laser beam scans laterally across the substrate, Marangoni forces push the polymer film away from the beam focus. (b) Optical microscope image of a polystyrene on silicon film that has been partially cleared by the plough effect. Scale (75 x 90 μm).

This effect extends the lateral scaling capability of the lithography process, enabling the patterning of structures much wider than the typical stationary thermal distribution. However, while the plough effect can create trenches much wider than that accessible with a single pass, the distance over which the laser can effectively push material has a limitation—Thicker films quickly build up a substantial ridge with a large contact angle. These steep sidewalls offer resistance to the Marangoni effect, which can result in an incomplete removal of the film. Figure 4.21 is an example of an extreme case, where the film was simply pushed around inside the square instead of being swept to the perimeter.

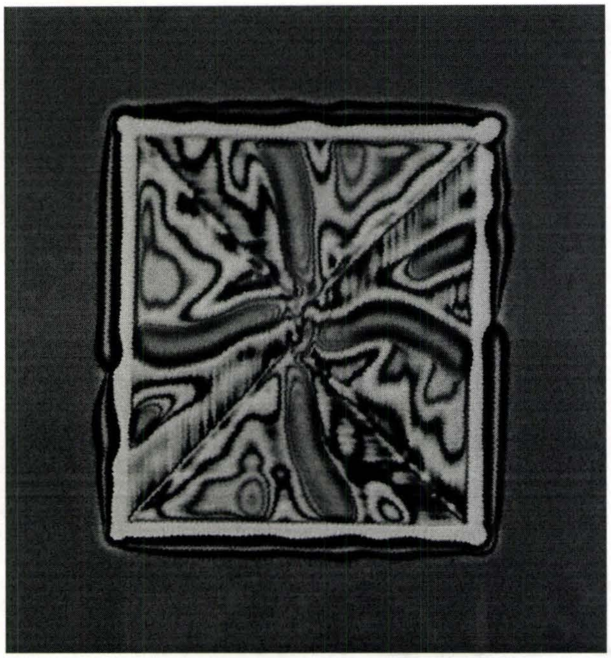

Figure 4.21: Optical image of an incomplete removal of a PS film on silicon with the plough effect. Scale (50 x 50 μm).

Fortunately, this hurdle can be overcome with number of procedural changes: Slowing down the scan speed of the laser gives the thermocapillary effect more time to exert its force and move material. The surface driving force can be strengthened by increasing the laser power and by increasing the size of the beam focus. These adjustments widen the thermal distribution and extend the lateral influence of the thermocapillary effect. Additional improvements in film removal are obtained by decreasing the increment distance between subsequent scans as well as repeatedly passing the laser across the same path. Applications of the plough effect for surface patterning will be further explored in Chapter 5.

4.7 Dewetting Enhanced Lithography

The thermal stability of thin liquid layers on surfaces is of great technological importance that spans a broad field of applications in the semiconductor, pharmaceutical, medical and pulp and paper industry [35]. Wetting (or dewetting), which refers to how a liquid deposited onto a surface spreads (or contracts), is an interesting phenomenon of thin film science that can be used to advantage to enhance the lithographic processing of thin polymer films.

Polystyrene is a material that dewets on silicon when its temperature is raised above its glass transition. This process occurs more readily if the substrate is first coated with thin layer of PDMS. PDMS is a polymer material with a very low surface tension that readily coats many surfaces that it comes into contact with. When placed in between a film of polystyrene and a substrate, it creates an interface that is much less favourable for the PS melt to exist on, which greatly enhances the drive to dewet. PDMS substrates are prepared by spin coating, at very low accelerations and speeds (500 rpm), a filtered 50% solution of PDMS in toluene onto carefully cleaned silicon. The samples are then annealed at 150°C for 1 hour in vacuum and then rinsed with toluene, leaving behind a very thin PDMS layer coating adsorbed onto the substrate. The polystyrene films are then deposited following the usual sample preparation procedures.

4.7.1 Rayleigh Instabilities of Thin Ribbons

Controlling the dewetting process on surfaces is an increasingly important requirement for modern technologies [36-37]. Some truly remarkable phenomena can be observed with lithography patterned films. A PS film on a PDMS coated Si substrate was patterned by laser lithography by scanning in a series of equally spaced trenches. The sample was then placed onto a heating stage and slowly raised above its glass transition temperature. Monitoring the film under an optical microscope reveals the time evolution of the dewetting process, shown in Figure 4.22. In its liquid state, the film naturally begins to dewet, leaving behind a series of thin liquid ribbons in the regions between the laser trenches. Being unfavourable at this elevated temperature, eventually the thin ribbons also begin to break up into a series of isolated droplets (known as the Rayleigh instability [17]).

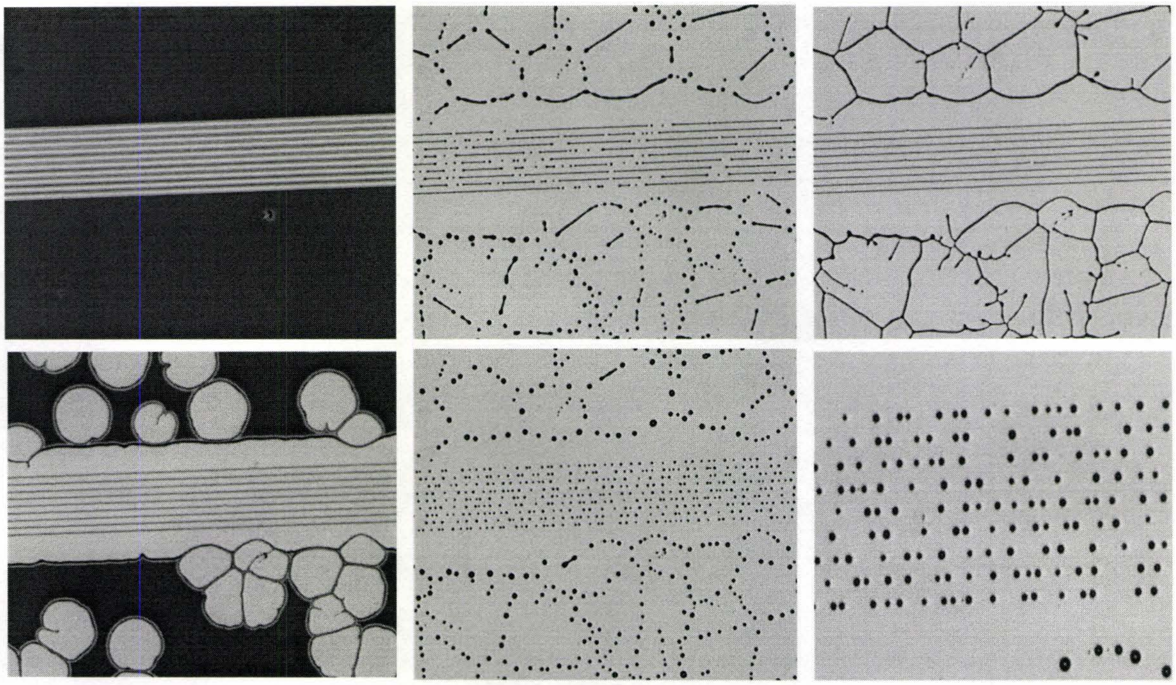

Figure 4.22: Dewetting time evolution of a laser patterned film of PS on PDMS on Si at 150°C. The thin ribbons of fluid bead up along the length of the laser trenches according to the Rayleigh instability. Scale (750 x 1050 μm), final image scale (200 x 280 μm). Sequence courtesy of J. Jarecki.

By varying the distance between the adjacent laser scans, different dewetting morphologies are observed. The following sequence of pictures (Fig. 4.23) depicts the time evolution of a series of thin, triangular ribbons that have been drawn into a film of PS on Si and PDMS.

The thin ribbons once again break up and form droplets ordered along the direction of the laser scan, but more interestingly, it appears that the laser trenches behave like a barrier to the dewetting film; the dewetting pattern becomes confined to the regions between the laser scans.

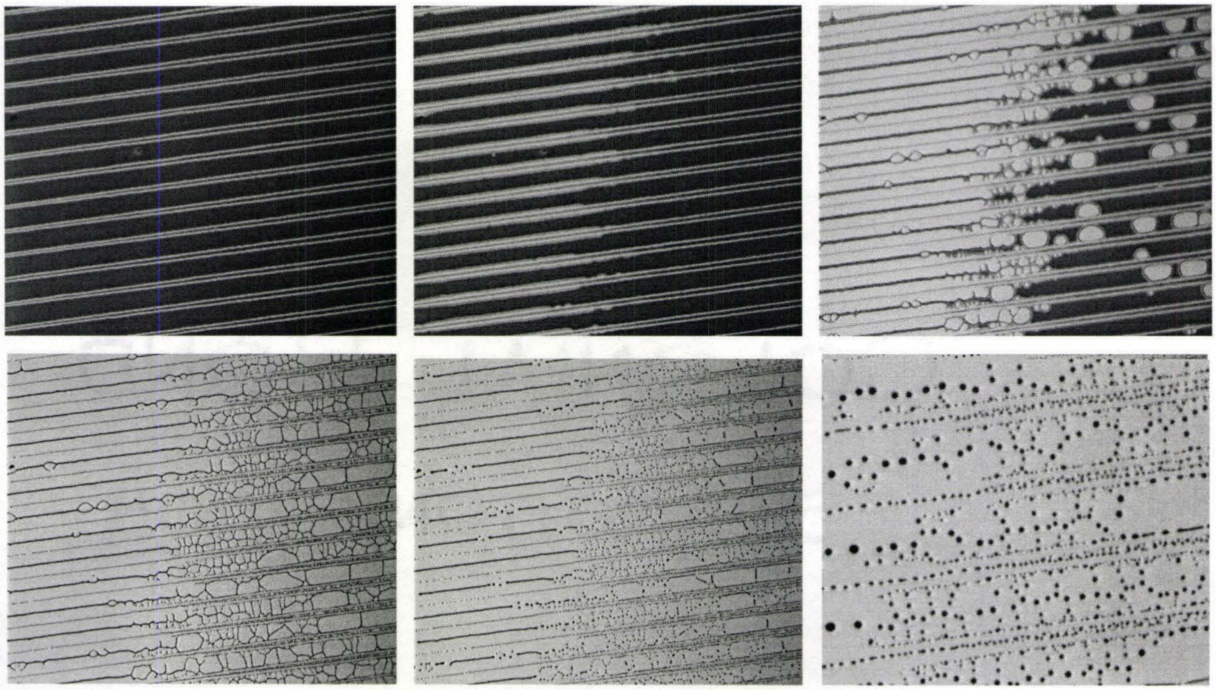

Figure 4.23: Dewetting time evolution of a laser patterned (triangular wedge) film of PS on PDMS on Si at 150°C. Lithography patterning is seen to control and confine the dewetting process. Scale (480 x 675 μm), final image (150 x 210 μm). Sequence courtesy of J. Jarecki.

Chapter 5

Applications of the Marangoni Effect

The ability to manufacture 3D structures on the surface of a polymer thin film with micron and nanometre scale resolution is one of the major advantages of the described Marangoni driven lithography system. With simple and relatively inexpensive components and materials, a wide variety of useful devices can be created, spanning the fields of physics and biology. This chapter will begin by presenting a brief review of two potential applications of the lithography system and concluded with a display of some of the more interesting patterns created over the course of the project.

5.1 Micro-Optics Array

In section 4.5 we saw how the dewetting of a thin polymer film could be controlled by first patterning the film with laser lithography. This phenomenon can be used to advantage to manufacture a periodic array of monodisperse polymer droplets, shown in Figure 5.1. A grid is patterned into a thin film of PS on a PDMS coated silicon substrate by scanning a focused laser across its surface (Figure 5.1 (a)). The pattern consists of an array of equally spaced and sized squares, whose dimensions are determined by the lithography process. The sample is then placed onto a heating stage and raised above the film's glass transition temperature. The isolated squares dewet into a periodically ordered array of spherical caps, with volumes equivalent to that of the original square film. One could imagine using such pattern as an array of micro-lenses for a combinatorial micro-optic experiment.

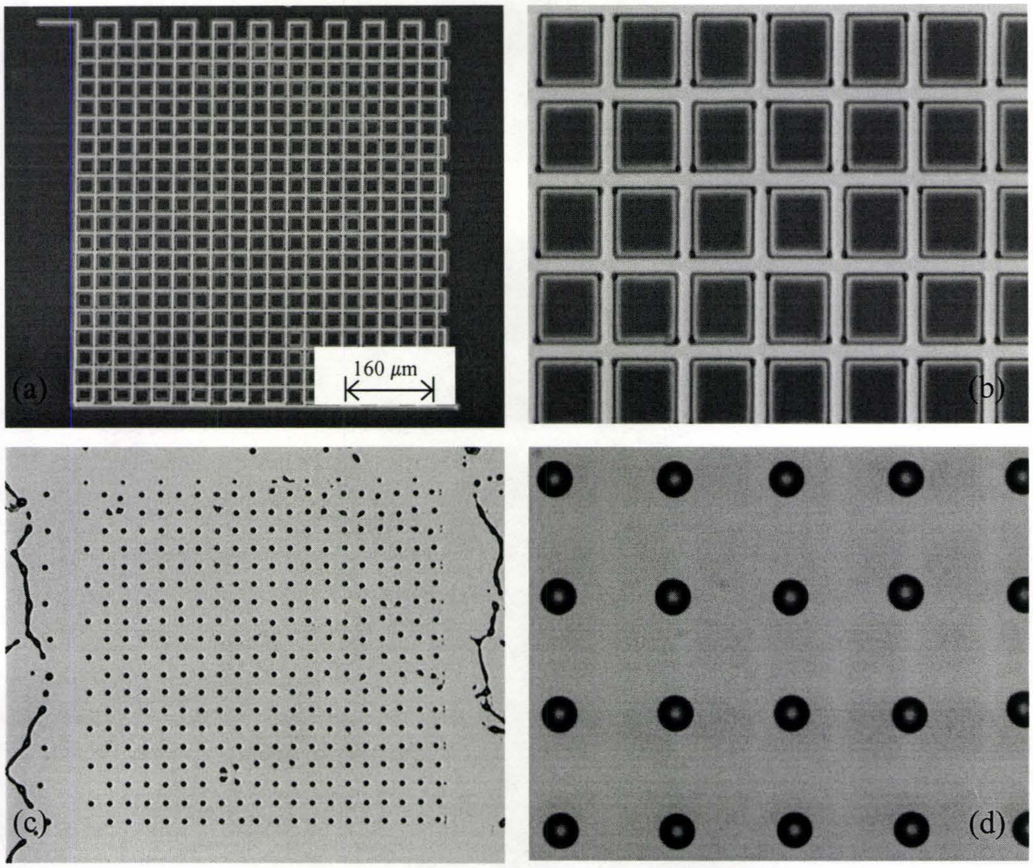

Figure 5.1: Grid patterns cut into a thin film of PS on PDMS coated Si dewet when raised above the glass transition temperature. The resultant pattern is an array of equally spaced, monodisperse spherical microcaps.

The surface profile of the caps can be inferred with knowledge of the volume of the cap, V_{cap}, given by the volume of the initial square V_{sq}, and the contact angle α that the cap makes with the substrate surface. The volume of the square is simply:

$$V_{sq} = l^2 \cdot h\,, \tag{5.1}$$

where h is the initial film thickness and l the spacing between the laser scans. The volume of the spherical cap is given by [38]:

$$V_{cap} = \left(\frac{\pi R^3}{3}\right)\cdot\left(2 - 3\cos(\alpha) + \cos^3(\alpha)\right) = l^2 \cdot h\,, \tag{5.2}$$

where the contact angle α and radius R are defined in Figure 5.2. The contact angle is system specific and can be determined by a number of standard methods (see ref. [11]).

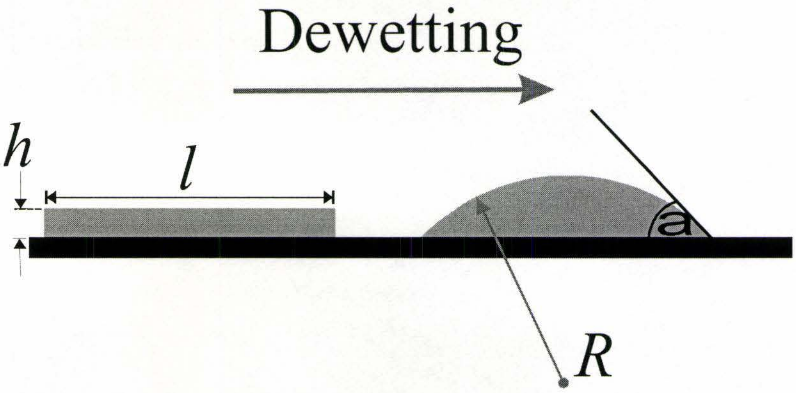

Figure 5.2: Schematic illustration of a square of dimensions *l* and *h* dewetting into a spherical cap with contact angle α and radius R.

By solving equation (5.2) for the radius *R*, the focal length *f* of the microlens can be determined from the following [18]:

$$f = \frac{n_m}{n_f - n_M} \cdot R, \tag{5.3}$$

where n_f and n_M are the refractive indices of the film and surrounding medium.

5.2 Microfluidic Devices

The manipulation of fluids on an extremely small length scale, otherwise known as *microfluidics,* is becoming an increasingly popular area of research and engineering. Owing to the dimensions of these devices, chemical reactions and composition analysis can be performed much more rapidly than with conventional macroscopic laboratory techniques. This increase in speed and the miniaturization of the components will help push the boundaries of biotechnology. Some current applications of microfluidic technology include DNA sequencing, sorting of cells, drug screening as well as research on genomics and proteomics [39-40]. An ultimate 'Holy Grail' of microfluidics is to integrate and condense entire laboratories onto a single substrate (labs-on-a-chip), leading to drastic improvements in throughput and cost.

Marangoni driven laser lithography on polymer films provides a simple means to fabricate microfluidic devices without the need for extensive (and expensive) fabrication infrastructure. Intricate networks of trenches and holes can quickly be patterned with micron and nanometre resolution, forming the channels and reservoirs of the composing microfluidic devices. While our laboratory has only recently entered the field of microfluidics, great efforts have led to the completion of a first prototype design, pictured in Figure 5.3.

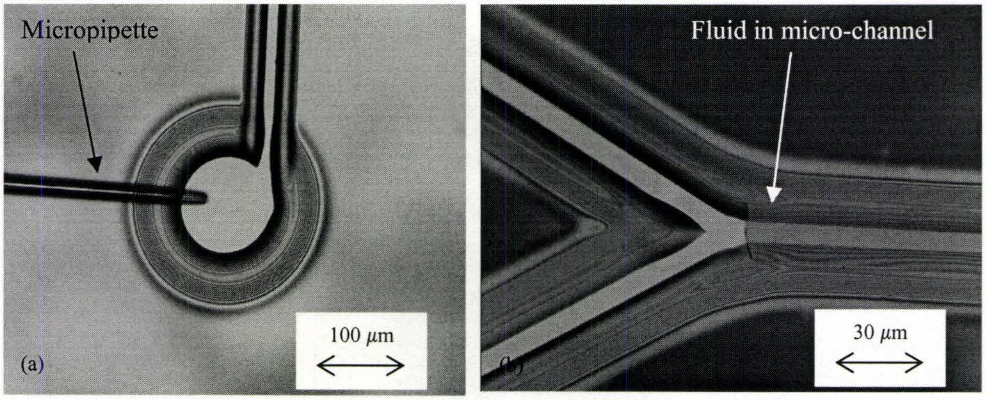

Figure 5.3: Optical microscope image of a capped polystyrene microfluidic reservoir (a) and 'Y' channel (b). Interfacing with the external world is accomplished by inserting a micropipette into the micro-reservoir, which is then fastened to a glass mount and coupled to external tubing. Images courtesy of M. Lee.

Current efforts are being directed towards the development and improvement of a systematic fabrication process and overcoming the issues surrounding the connections and seals with the external pump. Future endeavours will include the study of the fundamental behaviour of fluids in small channels as well as implementing complex pattern geometries in order to study the interaction of multiple flows and liquids.

5.3 Additional Patterns

The versatility of the lithography system to quickly create novel patterns is one of the most attractive features of the technology. This chapter will conclude with a brief illustration of some of the more interesting produced patterns.

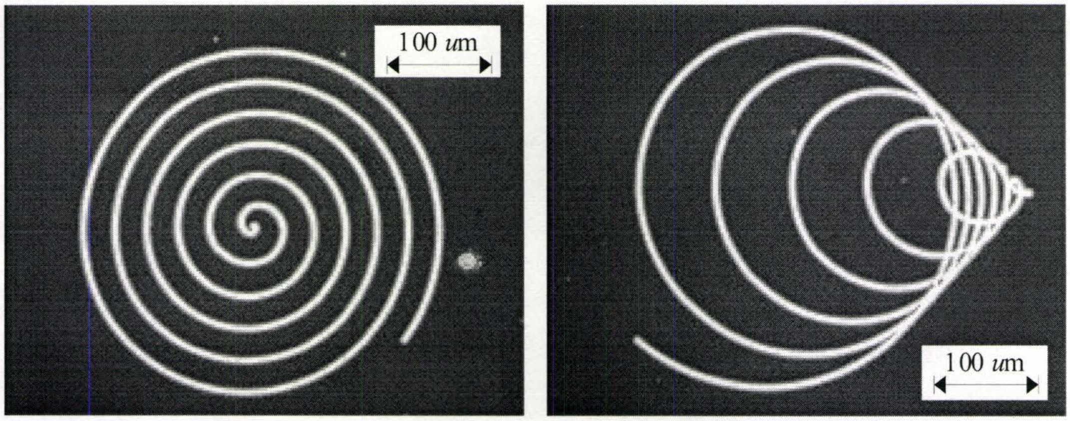

Figure 5.4: Spiral channels in a polystyrene film. Images courtesy of J. Parete.

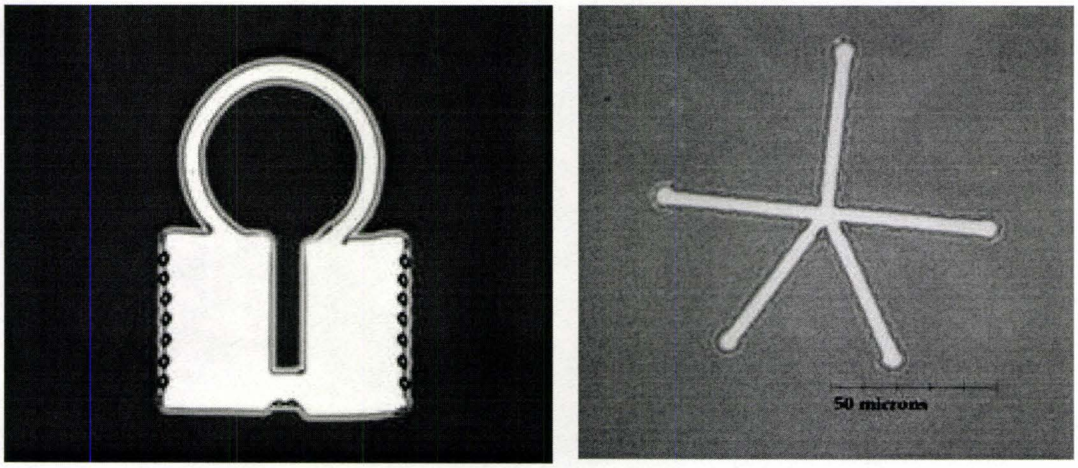

Figure 5.5: (a) Potential microfluidic switch and (b) interconnecting microfluidic channels. Images courtesy of J. Parete.

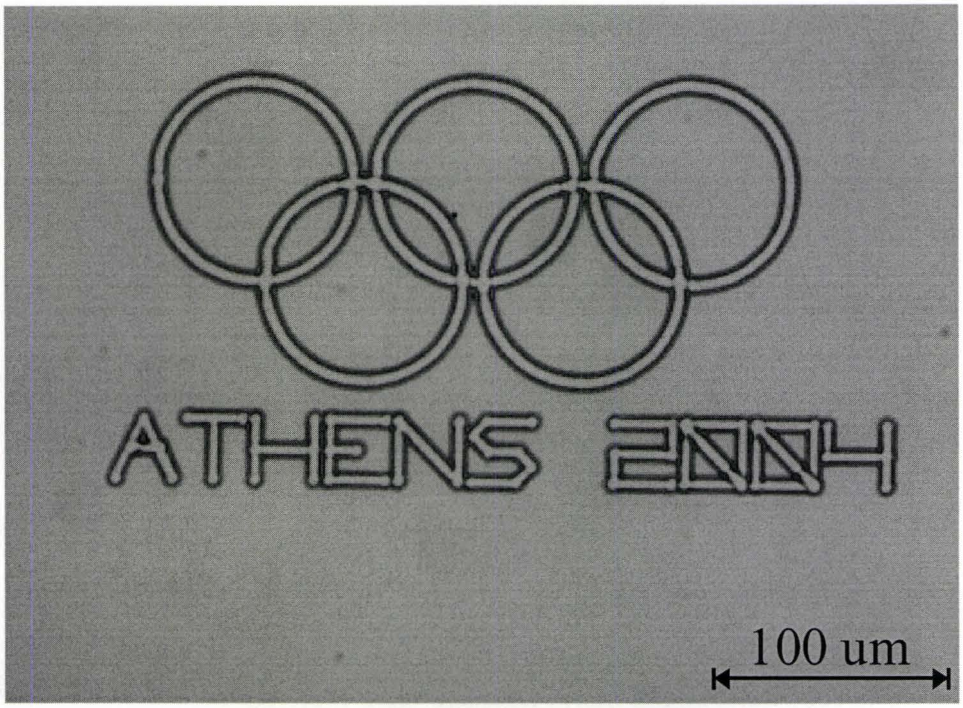

Figure 5.6: Our lab proudly supports our Canadian athletes, one micron at a time. Images courtesy of J. Parete.

Chapter 6

Conclusions

When a temperature gradient is imposed onto the surface of a liquid, the temperature dependence of the surface tension gives rise to a flow of material from the region of low surface tension that that of high surface tension; this is known as the Marangoni or thermocapillary effect. For the work presented in this thesis, a tightly focused laser beam has been used to induce sharp thermal gradients, exceeding 1,500,000 °C/cm, on the surface of thin polymer films. This process can be used to rapidly write trenches and patterns in the polymer films with fine control over their spatial dimensions and features (width, depth, etc.).

A presented hydrodynamic model, based on simple fluid mechanics, describes in a general sense the significance of time, incident power and film thickness on the observed behaviour of a thin polymer melt under the influence of a laser generated temperature gradient. However, the details of the individual evolution profiles reveal anomalous behaviours. It has been shown that this complex behaviour can be (in part) explained by considering the optical interference effects of the thin film coating. An optical feedback control loop has been developed to compensate for the interference effect by monitoring and maintaining a constant absorbed laser power. This ensures that the temperature gradient that drives the lithography process is consistent over the operation period.

At this point, the direction of future research can proceed along a number of different paths: The study of high laser powers interacting with films has revealed further anomalous behaviour, inconsistent with previous low to moderated power observations. The integration of block copolymers as a patterning material will merge the micron-sized structure of the lithography process with the nanometre scale features of the copolymer morphology. Lithography processes can also be enhanced by exploiting other thin film phenomena, such as dewetting, to create periodically ordered and controlled structures. However, perhaps the most useful extension of the project will be in the further development of microfluidic devices that will enable study of fundamental fluid behaviours in confined channels.

In essence, the completion of this project has only revealed the tip of the iceberg. Hopefully, it will later be reminisced as the small snowball that inevitably sparked an avalanche of future scientific discoveries and technological applications.

References:

[1] Bauerle, D., Laser Processing and Chemistry 3rd ed., (Springer, New York 2000)

[2] Chen, Y., Pepin, A., Electrophoresis, **22**, 187 (2001)

[3] Geoghegan, M., Krausch, G., *Wetting at polymer surfaces and interfaces*, Pro. Polym. Sci., **28**, 261 (2003)

[4] Massa, M., *Crystalization Kinetics and Crystal Morphology in Thin Poly(Ethylene Oxide) Films*, M.Sc. Thesis, (McMaster University 2002)

[5] Dalnoki-Veress, K., Dutcher, J.R. & Forrest, J.A., *Dynamics and Pattern Formation in Thin Polymer Films*, Phys. Can., March (2003)

[6] Seymour, R.B. *Structure-Property Relationships in Polymers*, (Plenum: New York 1984)

[7] Faber, T.E., *Fluid Dynamics for Physicists*, (Cambridge University Press: New York 2001)

[8] Strobl, G., *The Physics of Polymers: Concepts for Understanding Their Structures and Behavior 2nd ed.*, (Springer, New York 1997)

[9] Mark, J.E., *Physical Properties of Polymers Handbook*, (American Institute of Physics: New York 1996)

[10] Brandrup, J., Immergut, E.H. and Grulke, E.A., *Polymer Handbook, 4th Ed.*(Wiley: New York, 1989)

[11] De Gennes, P., Brochart-Wyart, F., Quere, D., *Capilarity and Wetting Phenomena: Drops, Bubbles, Pearls, Waves,* (Springer: New York 2002)

[12] Wu, S., *Surface and Interfacial Tensions of Polymer Melts. II.* J. Phys. Chem., **74**, 632 (1970)

[13] Molenkamp, T., *Marangoni Convection, Mass Transfer and Microgravity*, Ph.D. Thesis (University of Groningen, 1998) [online] http://www.desc.med.vu.nl/Publications/Thesis/Molenkamp/Molenkamp.htm

[14] Longtin, J.P., Hijikata, K., Ogawa, K., *Laser-induced surface tension-driven flows in liquids*, Int. J. Heat. Mass. Transfer, **42**, 85 (1999)

[15] Coherent Laser Group, *Operator's Manual: Verdi V-2/V-5. Diode Pumped Lasers*

[16] Edmund Optics, [online Catalog] http://www.edmundoptics.com/onlineCatalog/browse.cfm

[17] Pedrotti, F.L., Pedrotti, S.J.L., *Introduction to Optics 2^{nd} ed.,* (Prentice Hall:, New Jersey 1993)

[18] Hecht, E. *Optics 3^{rd} ed.,* (Addison-Wesley: New York 1998)

[19] Rantala, T.T., & Levoska, J., *A numerical simulation method for laser induced temperature distributions*, J. Appl. Phys., **65,** 4475 (1989)

[20] Ravindra, N.M., et al. *Modelling and Simulation of Emissivity of Silicon-Related Materials and Structures*. J. Elect. Mat, **32,** 1052 (2003)

[21] Lax, M., Temperature rise induced by a laser beam., J. Appl. Phys., **48**, 3919 (1977)

[22] Lax, M., Temperature rise induced by a laser beam II. The non linear case, J. Appl. Phys., **33**, 786 (1978)

[23] Moody, J.E., Hendel, R.H., *Temperature profiles induced by a scanning cw laser beam,* J. Appl. Phys., **53**, 4364 (1982)

[24] Levoska, J., Rantala, T.T., Lenkkeri, J., *Numerical simulation of temperature distributions in layerd structures during laser processing,* Appl. Surf. Sci., **36**, 12 (1989)

[25] Ashcroft, N.W., Mermin, N.D., *Solid State Physics*, (Harcourt, New York 1976)

[26] Ho et al., *Thermal conductivity of the elements: a comprehensive review,* J. Phys. Chem. Ref. Data, **3** [Suppl. 1], 588 (1974)

[27] Jellison G.E., Modine F.A., *Optical functions between 1.7 and 4.7 eV at elevated temperatures,* Phys. Rev. B, **27**, 7466 (1983)

[28] Berns, M.W., *Laser scissors and tweezers*, SCIAM, April 1998.

[29] Savage, S., *Introduction to light forces, atom cooling and atom trapping*, Aust. J. Phys., **49**, 745 (1996)

[30] Guck, J. et al., *Optical deformability of soft biological dielectrics*, PRL, **84**, 5451 (2000)

[31] Ashkin, A., Dziedzic, J.M., *Radiation pressure on free liquid surface*, PRL, **30**, 139 (1973)

[32] Fowles, G.R., *Introduction to Modern Optics 2^{nd} ed.,* (Dover: New York 1989)

[33] F.S. Bates and G.H. Fredrickson, *Block Copolymers—Designer soft materials, Physics Today*, **52**, 32 (1999)

[34] Muthakumar, M., Ober, C.K., Thomas, E.L., *Competing interactions and levels of ordering in self-organized polymeric materials*, Science **277**, 1225 (1997).

[35] Hatsopoulos Microfluids Laboratory [online]:
http://web.mit.edu/agrawala/www/NIRT/wetting.html

[36] E. Meyer & H.G. Braun, *Controlled dewetting processes on microstructured surfaces – a new procedure for thin film microstructuring,* Macromol. Mater. Eng., **276/277**, 44 (2000)

[37] G. Reiter *Dewetting of Thin Polymer Films*, PRL, **68**, 75 (1992)

[38] Gokhale, S.J. et al., *Experimental investigation of contact angle, curvature, and contact line motion in dropwise condensation and evaporation,* J. Col. Int. Sci. **259**, 254 (2003)

[39] Pfohl, T. et al., *Trends in microfluidics with complex fluids*, CHEMPHYSCHEM, **4**, 1291 (2003)

[40] Whitesides, G.M., Stroock, A.D., *Flexible methods for microfluidics*, Phys. Today, **42** (June 2001)

Appendices

A Photonic Forces

B Lensing Effect

Appendix A:

Photonic Pressure

Estimating the resultant pressure of a light ray on a polymer film is accomplished as follows:

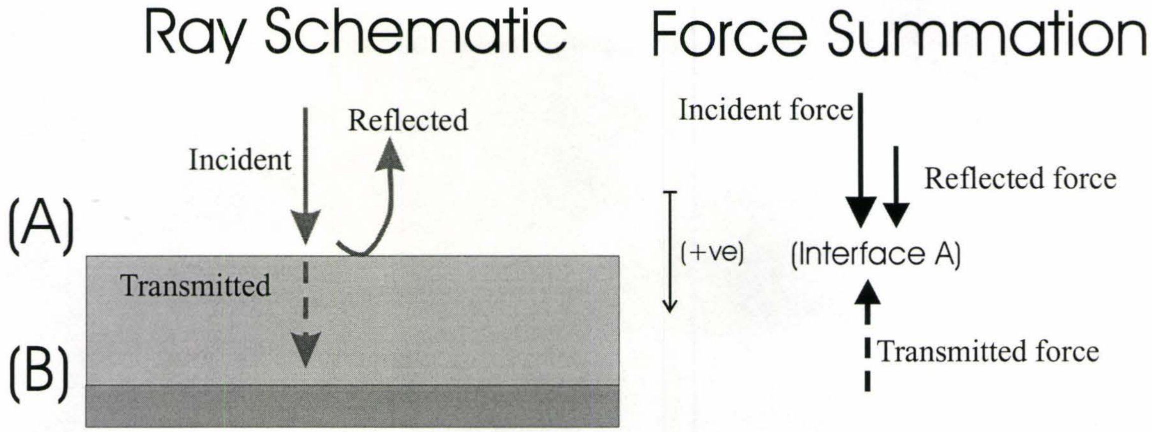

At normal incidence, the % of reflected power is given by:

$$R = \left(\frac{1-n}{1+n}\right)^2 \tag{A1.1}$$

where

$$n = n_2 / n_1$$

Thus, at interfaces (A) and (B), the reflectance is respectively:

$$R_A = \left(\frac{1-1.512}{1+1.512}\right)^2 = 0.042 \text{ AND } R_B = \left(\frac{1-2.65}{1+2.65}\right)^2 = 0.020 \tag{A1.2}$$

The force F of a beam of power P_o incident on a surface is given by:

$$F_m = \frac{n_m}{c} P_o ; \tag{A1.3}$$

where n_m is the refractive index of the initial medium and c, the speed of light in vacuum.

Consider interface (A):

When the incident ray strikes the surface (A), it is both partially reflected and transmitted. The incident ray exerts a force along the direction of propagation. The reflected and transmitted rays exert a recoil force in the opposite direction of their resultant paths owing to their change in momentum. With the coordinate system defined downward as positive, the net force at interface (A) is given by:

$$F_{NET,A} = \frac{P_o}{c}\left[n_m + R_A \cdot n_m - n_f(1-R_A)\right] \tag{A1.4}$$

Consider interface (B):
At interface (B), now with a reduced power of $P_o(1\text{-}R_A)$, the ray is partially reflected back towards the film/air interface. Summing the forces of a ray of power $P_o(1\text{-}R_A)R_B$ incident from below the interface…

$$\begin{aligned} F_{NET,B} &= \frac{P_{incident}}{c}\left[-n_f - n_f R_A + n_m(1-R_A)\right] \\ &= \frac{P_o(1-R_A)R_B}{c}\left[-n_f - n_f R_A + n_m(1-R_A)\right] \end{aligned} \tag{A1.5}$$

Taking the values of n_m, n_f and n_s as 1, 1.5 and 4.1 respectively (representing air, polystyrene and silicon), one immediately sees that the direction of the net force is upwards, for both (A1.4) and (A1.5). Thus, the influence of any radiation pressure effects would cause the surface of a polymer film to bulge away from the substrate in the direction opposite of the observed lithography patterns.

Appendix B:

The Lensing Effect

Approximating the curvature of a dimple to be spherical, the refraction of a normally incident laser beam of radial width *w*(*h*) is calculated for the hole geometry depicted below.

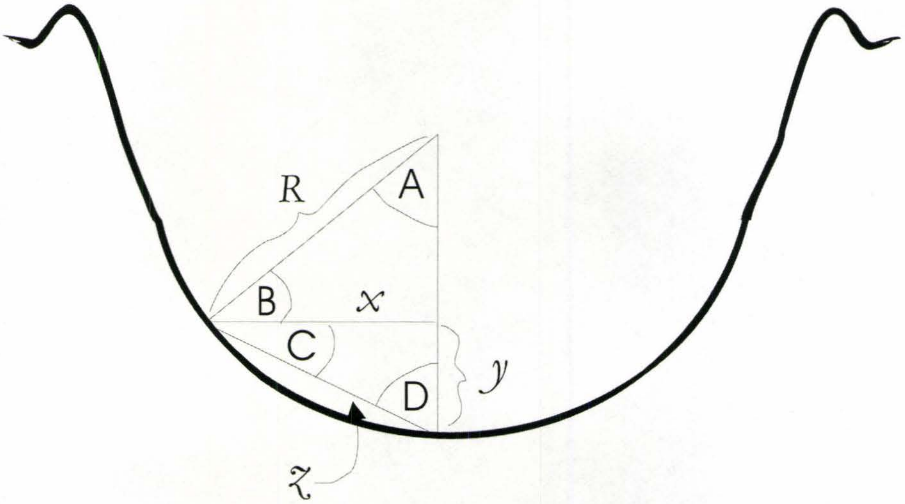

The aspect ratio x/y can be measured from AFM cross sections. The radius of curvature *R* can then be calculated with some simple trigonometry:

Pythagorum theorem:

$$z = \sqrt{x^2 + y^2} \tag{B.1.1}$$

Simple trigonometry:

$$\tan D = \frac{x}{y}$$

$$D = \tan^{-1}\left(\frac{x}{y}\right) \tag{B.1.2}$$

Law of sines:

$$\frac{\sin A}{z} = \frac{\sin D}{R} = \frac{\sin(B+C)}{R} \tag{B.1.3}$$

$$\therefore D = B + C$$

Conservation of angles:

$$A = 180^\circ - D - (B+C)$$

$$A = 180^\circ - 2D \tag{B.1.4}$$

Combining

$$\frac{\sin(180-2D)}{z} = \frac{\sin(D)}{R}$$

$$R = \frac{z \cdot \sin(D)}{\sin(180-2D)} \tag{B.1.5}$$

From the thin lens equation, the focal length *f* of a lens imitating the dimensions of Figure A1.1 can be determined:

$$\frac{1}{f} = \frac{n_2 - n_1}{n_1} \cdot \left(\frac{1}{R_1} - \frac{1}{R_2}\right) \tag{B.1.6}$$

For

$n_1 = 1$
$n_2 = 1.5$
$R_1 = \infty$
$R_2 = 1 \text{ x } 10^{-4}$ m

$$\frac{1}{f} = \frac{1.5-1}{1} \cdot \left(\frac{1}{\infty} - \frac{1}{0.0001}\right)$$

$$f = -5000 \text{ m} \tag{B.1.7}$$

$\therefore$ The focal length of the hole with the calculated curvature *R* is 5000 m (divergent). The effect this will have on the beam focus at the film/substrate interface can be determined from simple trigonometric arguments.

Assuming that the beam is maximally focused at the film substrate interface, the beam waist will be slightly broader at the air/film interface due to divergence. We can estimate the beam waist a distance *h* from the substrate surface from:

$$w^2(h) = w_o^2 \cdot \left[1 + \left(\frac{\lambda \cdot h}{\pi \cdot w_o^2}\right)^2\right] \tag{B.1.8}$$

Given

$\omega_o = 3.06\ \mu\mathrm{m}$
$\lambda = 532\ \mathrm{nm}$
$h = 200\ \mathrm{nm}$

$$w\ (h) = \left(3.06\times10^{-9}\right)\sqrt{\cdot\left[1+\left(\frac{532\times10^{-9}\cdot200\times10^{-9}}{\pi\cdot\left(3.06\times10^{-9}\right)^{2}}\right)^{2}\right]} \approx 3.19\ \mu\mathrm{m} \qquad \text{(B.1.9)}$$

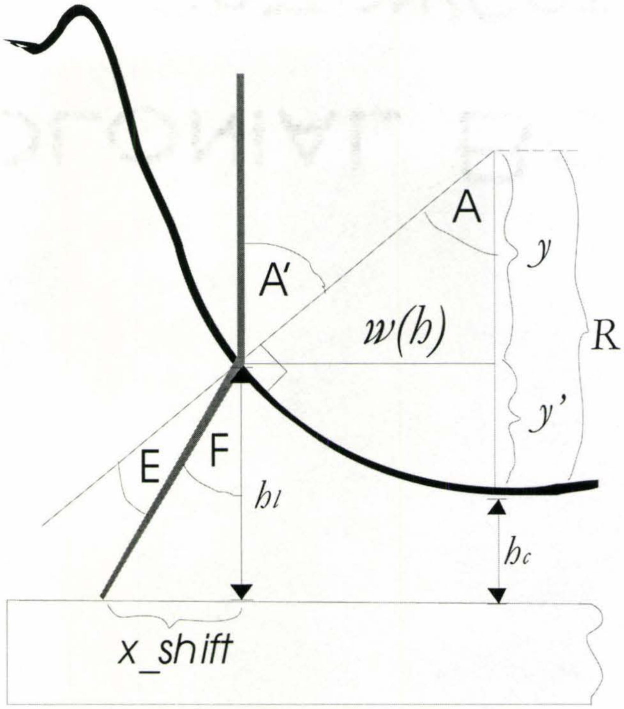

By considering a normally incident ray a distance $w(h)$ from the center of the profile, the lateral refraction shift (*x_shift*) can be determined:

Snell's Law predicts:

$$n_1 \sin(A') = n_2 \sin(E) \tag{B.1.10}$$

Re-arranged as:

$$E = \sin^{-1}\left(\frac{n_1}{n_2}\sin(A')\right) \tag{B.1.11}$$

Simple trigonometry yields:

$$A = \tan^{-1}\left(\frac{w(h)}{R}\right) \tag{B.1.12}$$

From conservation of angle,

$$\begin{aligned} A &= E + F \\ \therefore F &= A - E \end{aligned} \tag{B.1.13}$$

Finally,

$$\tan(C) = \frac{x}{h_l} \tag{B.1.14}$$

Since the film height is slightly thick a distance *w*(*h*) from the center of the lens, h_l is determined as follows:

$$y = \sqrt{R^2 - w(h)^2} \tag{B.1.15}$$

$$y' = R - y \tag{B.1.16}$$

$$h_l = h_c + y' \tag{B.1.17}$$

The final shift in the focused beam is:

$$x\_shift = h_l \cdot \tan(C) \tag{B.1.18}$$

Numerical Estimation

It is not uncommon for dimples to form with aspect ratios greater than 100. The beam divergence for such a dimple is now estimated. (Italicized represent calculated values)

x = 2.00E-06
y = 2.00E-08
z = 2.0001E-06

Refractive index
n1 = 1
n2 = 1.5

	Radians	**Degrees**
D =	*1.5607966*	*89.42706*
R =	*0.00010*	

Film thicknesses
hc 2.00E-07
hl 2.46E-07

Approximate width of a laser beam h distance from the surface of the substrate…

h = 2.00E-07
w_o = 3.02E-06
λ = 5.32E-07

w(h) = 3.2E-06

x_shift = 2.62E-09 [m]

The influence of the profile curvature broadens the radius of the beam by ~ 3 nm. For a beam waist $\omega_o = 3.0$ μm, this represents a 0.1 % change.